



Deposited via The University of Leeds.

White Rose Research Online URL for this paper:

<https://eprints.whiterose.ac.uk/id/eprint/169434/>

Version: Accepted Version

Article:

Zhao, Y, Hua, Y, Liu, B et al. (2021) The development of a Mechanistic-Chemometrics model with multi-degree of freedom for pitting corrosion of HP-13Cr stainless steel under extremely oilfield environments. *Corrosion Science*, 181. 109237. ISSN: 0010-938X

<https://doi.org/10.1016/j.corsci.2021.109237>

© 2021 Elsevier Ltd. This manuscript version is made available under the CC-BY-NC-ND 4.0 license <http://creativecommons.org/licenses/by-nc-nd/4.0/>.

Reuse

This article is distributed under the terms of the Creative Commons Attribution-NonCommercial-NoDerivs (CC BY-NC-ND) licence. This licence only allows you to download this work and share it with others as long as you credit the authors, but you can't change the article in any way or use it commercially. More information and the full terms of the licence here: <https://creativecommons.org/licenses/>

Takedown

If you consider content in White Rose Research Online to be in breach of UK law, please notify us by emailing eprints@whiterose.ac.uk including the URL of the record and the reason for the withdrawal request.

1 **The development of a Mechanistic-Chemometrics model with**
2 **multi-degree of freedom for pitting corrosion of HP-13Cr stainless**
3 **steel under extremely oilfield environments**

4

5 Yang Zhao¹, Yong Hua², Bin Liu³, Xuanpeng Li^{4*}, Junfeng Xie⁵, Guanxin Zeng⁵, Tao
6 Zhang^{1*}, Fuhui Wang¹

7

8 *¹Shenyang National Laboratory for Materials Science, Northeastern University, 3-11*
9 *Wenhua Road, Shenyang 110819, China.*

10 *²Institute of Functional Surfaces, School of Mechanical Engineering, University of*
11 *Leeds, Leeds, LS2 9JT, United Kingdom.*

12 *³Corrosion and Protection Laboratory, Key Laboratory of Superlight Materials and*
13 *Surface Technology, Harbin Engineering University, Ministry of Education, Nantong*
14 *ST 145, Harbin 150001, China.*

15 *⁴ State Key Laboratory of Performance and Structural Safety for Petroleum Tubular*
16 *Goods and Equipment Materials, Tubular Goods Research Institute, CNPC, Xi'an*
17 *710077, China*

18 *⁵ Petrochina Tarim Oilfield Company, Shihua RD, Korla 841000, China.*

19

20 Corresponding authors: Xuanpeng Li (lixuanpeng127@163.com); Tao Zhang
21 (zhangtao@mail.neu.edu.cn).

22

23 **Abstract**

24 A multi-degree of freedom mechanistic-chemometrics model for predicting the pitting
25 damage of HP-13Cr stainless steel is developed by combining the mechanistic models
26 and chemometrics method. The mechanistic model is reconstructed by considering the
27 effect of single factors, such as high temperature, high CO₂ pressure, flow rates and
28 complex stress distribution. The single mechanistic models are combined together
29 considering the weight coefficients of variable interaction using the chemometrics
30 method. Finally, the predicted results are validated by six-year-served field data,
31 which indicates that the newly developed mechanistic-chemometrics model is
32 accurate and highly reliable.

33

34 **Keywords:** A. Stainless steel; B. Modeling studies; B. Polarization; C. Pitting
35 corrosion

36

37

38

39

40

41

42

43

44

45 **1. Introduction**

46 The increasing demand for resources has shifted the exploration towards ultra-deep
47 oil wells at Tarim oilfield in the Northwest of China. Due to the complicated
48 downhole conditions and geological characteristics in Tarim area [1-3], Oil Country
49 Tubular Goods (OCTG) are in the oilfield environment (as depicted in Fig. 1). Fig. 1
50 represents the characteristics of complex oil-well environment, which is conducive to
51 corrosion and can be described as [4]:

52

53 (1) Super corrosive media: the well depth reached 8000 m, high temperature (95 -
54 180 °C), high CO₂ pressure (2.8 - 3.8 MPa). The measured water cut was more than
55 30%. Moreover, the formation water contains high salinity (Cl⁻ concentration is about
56 60, 000 ppm).

57

58 (2) Stress Corrosion Cracking (SCC) mechanism: A neutral point, with zero stress
59 above the packer, exists due to the gravity and mechanical properties of the structure
60 tubing. Meanwhile, the tensile stress is located above the neutral point, while the
61 stress transforms into compressive stress between the neutral point and the packer.
62 Later on, due to the gravity, the compressive stress transforms into tensile stress below
63 the packer [5].

64

65 HP-13Cr stainless steel (SS) is widely used as an OCTG in oil industry, as they offer
66 improved CO₂ corrosion resistance in relation to carbon steels, and offer lower costs

67 than the duplex SS grades or Ni alloys [6-10]. However, the inspected field results
68 have revealed that HP-13Cr SS suffers severe pitting corrosion. In general, the pitting
69 corrosion can be divided into two processes, namely the pit initiation and the pit
70 growth. The complex oilfield environment in terms of temperature, CO₂ pressure,
71 flow rate and stress can influence the pitting processes. Nesic et al. [11] reported that
72 temperature and CO₂ pressure accelerate the pitting corrosion by the electrochemical,
73 chemical, and transport processes. Additionally, the effect of temperature and CO₂
74 pressure on the pitting corrosion has been studied on passive films and corrosion
75 scales [6, 9, 10, 12-15]. The results illustrate that the enhanced pitting susceptibility of
76 HP-13Cr SS can be attributed to the effects of temperature and CO₂ pressure on the
77 microstructure and composition of corrosion scales [14]. In addition, Zhao et al. [15]
78 discussed the influence of temperature and CO₂ pressure on the growth of pit on
79 HP-13Cr SS. The results indicated that pit cavities grew deeper with the increase in
80 temperature and CO₂ pressure from 95 °C / 2.8 MPa to 180 °C / 3.8 MPa after being
81 immersed for 30 days.

82

83 Nesic et al. [11, 16] systematically studied the influence of flow rate on the carbon
84 steel pipeline in the presence of CO₂ corrosion. It has been acknowledged that, high
85 flow rate affects the CO₂ corrosion by increasing the mass transfer of corrosive
86 species as well as damaging the corrosion scales. Schmitt et al. [17] indicated that 0.2
87 Pa of wall shear stress was enough to induce pitting corrosion. Moreover, Xu et al.
88 [18] reported that flow rate can suppress the development of potential pits by

89 uniformly distributing ions at the interface of metal. Wharton et al. [19] reported that
90 the flow rate (0.04- 2.7 m/s) had a negligible influence on pit nucleation and
91 metastable pitting, whereas the growth of pits became obvious when the flow rate was
92 slower than 1.5 m/s. Furthermore, these experimental results were confirmed by
93 hydrodynamic and electrochemical noise measurements for AISI 304 SS. Wei et al.
94 [20] proposed that the flow rate (0.5-2 m/s) accelerated the pitting corrosion by
95 damaging the corrosion scales and inhibiting the formation of FeCO_3 on the surface of
96 X70 under supercritical CO_2 environment. Recently, Zhao et al. [15] demonstrated
97 that the flow rate altered the pitting geometry from bullet shape to shallow-disk shape
98 at the flow rate of 3 m/s.

99

100 Moreover, it has been reported that the applied tensile stress increased the pitting
101 susceptibility, whereas the compression stress could reduce the pitting susceptibility
102 [21-26]. Iwanaga et al. [26] performed polarization tests and reported that pitting
103 susceptibility of stainless steels increased with the increase in tensile stress. Vignal et
104 al. [27] demonstrated that the local tensile stress gradient played a key role in
105 accelerating the pit initiation process. Additionally, Feng et al. [28] proposed two
106 degradation modes for the passive film under tensile or compressive stress. The
107 results suggested that tensile stress produced micro-cracks, which were perpendicular
108 to the surface, whereas the compressive stress induced de-bonding of the passive film
109 from the steel substrate [28]. Moreover, Guo et al. [29] and Fatoba et al. [30] reported
110 that, based on Gutman model, the influence of tensile stress on the acceleration of

111 metastable pit and pit growth based on Gutman model can be attributed to the
112 mechanical-electrochemical effect at the local plastic deformation around the bottom
113 of the pit [31].

114

115 Significant progress has been achieved in understanding the effect of temperature,
116 CO₂ pressure, flow rate and stress on the pitting corrosion [32-33]. However, the
117 synergistic effect of these factors on pitting corrosion of HP-13Cr SS has not yet been
118 studied in detail. The development of a theoretical model to predict corrosion damage
119 of HP-13Cr SS in the extremely oilfield environments has become necessary. In
120 recent years, CO₂ corrosion has been extensively investigated to understand the
121 fundamental corrosion mechanism, whereas corrosion prediction models have also
122 been developed to predict the CO₂-induced corrosion for various steels [11]. The
123 current prediction models, including empirical models [34, 35], semi-empirical
124 models [36-38], and comprehensive mechanistic models [39-41], mainly focus on
125 CO₂-induced general corrosion of mild steel. It should be noted that the pitting
126 corrosion plays a major role in the failure of wells. Therefore, a significant research
127 effort has been devoted to predict the pitting corrosion using the stochastic model and
128 deterministic model [42-46]. Recently, Zhang' group [47] proposed a novel model to
129 predict the pitting corrosion, which considers the influence of the initiation and
130 growth of a pit. The proposed model was based on a combination of Sridhar model,
131 Macdonald model, Weibull extreme value statistics and Gumbel extreme value
132 statistics method. The proposed model was successfully applied to predict the

133 development of pitting at various times for 304 SS. However, the modelling became a
134 challenge for corrosion under complex coupling environments due to which, the
135 model required further reconstruction.

136

137 In addition, chemometrics method belongs to a discipline that provides an efficient
138 approach through statistical or mathematical methods to investigate the effect of each
139 variable and the interaction between variables [48-50]. A combination of chemometric
140 method and the model proposed by Zhang's group results in a novel
141 mechanistic-chemometric prediction model, which is developed herein in order to
142 incorporate the influence of temperature, CO₂ pressure, flow rate and stress on the
143 growth kinetics of pits. The model has then been used to perform pitting corrosion
144 calculations. In order to verify the accuracy of mechanistic-chemometric model, the
145 predicted results are compared with the field data of HP-13Cr SS well after being
146 used for six years in the Tarim area.

147

148 **2. Experimental**

149 **2.1 Materials**

150 HP-13Cr SS was used in the current study, and had the composition of (wt. %) Si
151 (0.15), Mn (0.51), Cr (12.77), Mo (2.19), S (0.002), P (0.02), Cu (0.047), Ni (5.36), V
152 (0.014), Al (0.037) and Fe (balance). The formation water was prepared by using the
153 analytical grade reagents and distilled water. The compositions of various materials
154 are listed in **Table 1**. The specimens of 50 mm × 5 mm × 3 mm (**Fig. 2 (a)**) were used

155 for the immersion and electrochemical tests under various temperatures and pressures.
156 As shown in Figs. 2 (b-d), the specimen had the dimensions of 32 mm × 10 mm × 1
157 mm and was designed to investigate the pit growth process under different flow rates,
158 tensile stresses and compressive stresses. In addition, based on the factorial design
159 method [51], heteromorphic electrode was used to determine the weight coefficient.
160 Prior to the testing, the specimen surface was ground by silicon carbide (SiC) paper
161 up to 2000 grit. The formation water was deoxygenated with N₂ for 4 h. Then, 3.5 L
162 formation water was introduced into the autoclave, sealed, and continuously bubbled
163 with CO₂ at ambient temperature and pressure for 2 h to remove oxygen in the
164 autoclave. Subsequently, the autoclave was heated to the required temperature, and
165 high-pressure CO₂ was added to the autoclave using a booster pump.

166

167 **2.2 Computational fluid dynamics and stress distribution**

168 Herein, computational fluid dynamics (CFD) simulation of the flow distribution of
169 heteromorphic electrode in the closed system was performed using the ANSYS
170 FLUENT 14.0. A simulation geometry was constructed based on the dimensions of
171 heteromorphic electrode and a tetrahedral computational 13000 element mesh was
172 generated. Reynolds number (Re) is about 64,000 were in this experiment based on
173 the fluid theory [52]. The SST $k-\omega$ turbulent model was used to approach the
174 governing equations with an enhanced wall treatment. A uniform velocity-inlet
175 boundary condition was selected, and a pressure-outlet boundary condition was set
176 with a gauge pressure of zero for the closed system. The iterative calculations of the

177 semi-implicit method for pressure-linked equations (SIMPLE) algorithm were used to
178 solve the momentum equations (N - S equations), which modified the pressure term in
179 the discretized N - S equations and simultaneously renewed the velocity and pressure
180 field. The simulations were converged when the minimum value reached less than
181 5×10^{-4} [52-53].

182

183 In addition, the stress distribution was carried out using the COMSOL
184 MULTIPHYSICS 3.5a. A static solid stress-strain isotropic elastic analysis module
185 was used to simulate the stress distribution of high throughput tensile stress
186 heteromorphic specimens. Based upon the literature, the maximum applied stress (350
187 MPa) was lower than the yield strength (800 MPa) [5, 54].

188 |

189 **2.3 Methods**

190 The influence of each factor was quantified by 2^3 factorial design [54]. The lower and
191 upper values for temperature/ CO_2 pressure, flow rate and stress were selected based
192 on the depth of well (Fig.1), and are presented in Table 2. The values of -1 and +1
193 indicated low and high levels for each factor. Meanwhile, after being immersed for
194 720 h, the maximum pitting depth (D_{\max}) of HP-13Cr SS was taken as the response.
195 The multiple regression analysis through least-squares method was used to describe
196 the relationship between the factors (x) and responses (D_{\max}). Moreover, the analysis
197 of variance (ANOVA) was performed to statistically evaluate the significance of
198 various factors. ANOVA was also used to test the null hypothesis. This method is

199 based on the decomposition of total variability in the selected response (y) and
200 assesses the relationship between the factors and the variability of responses. The
201 significant factors or interactions can be identified as the ratio of the mean square of a
202 factor or as an interaction and the residual mean square (F -value) [49-50]. If the
203 F -value was less than 11.27, the factors were considered as negligible [55].

204

205 2.4 Electrochemical characterization

206 The electrochemical measurements were carried out using a standard three-electrode
207 system within the high-temperature high-pressure autoclave, as reported in some
208 previous works [14-15]. HP-13Cr SS was used as a working electrode, whereas
209 platinum was used as a counter electrode. Furthermore, an external pressure balanced
210 Ag/AgCl was used as the reference electrode (0.1 M KCl solution). The electrode
211 potentials were converted to standard hydrogen electrode (SHE) potential using
212 Equation (1) [56].

$$213 \quad E_{SHE} = E_{obs} + 0.2866 - 0.001(T - T_0) + 1.754 \times 10^{-7}(T - T_0)^2 - 3.03 \times$$
$$214 \quad 10^{-9}(T - T_0)^3 \quad (1)$$

215 where E_{SHE} represents the electrode potential vs SHE, E_{obs} represents the measured
216 electrode potential vs the Ag/AgCl reference electrode (V), T refers to the
217 experimental temperature (°C) and T_0 denotes the room temperature (25 °C).

218

219 The specimens were potentiostatically polarized at -1.3 V_{SHE} for 3 min to remove the
220 surface oxide layer. The re-passivation potential (E_{rp}) was measured using the cyclic

221 potentiodynamic polarization measurements according to ASTM G61-86 [57]. The
222 cyclic potentiodynamic polarization curves were recorded from a potential of -100
223 mV vs the Open Circuit Potential (OCP). When the increased potential was up to a
224 current density of 1 mA/cm² with the scan rate of 1 mV/s, the scan was reversed to
225 obtain the E_{rp} . Then, the scan rates were changed through values of 0.5 mV/s, 0.333
226 mV/s and 0.167 mV/s. The temperature and pressure of electrochemical tests were
227 maintained at 95 °C/2.8 MPa, 120 °C/3.2 MPa, 150 °C/3.6 MPa and 180 °C/3.8 MPa.
228 For each electrochemical test, the measurement was repeated at least three times.

229

230 **2.5 Immersion tests**

231 Immersion experiments were performed in a 5-L high-temperature and high-pressure
232 autoclave. A schematic of the experimental setup can be viewed in our previous study
233 [15]. Similar to the previous study [15, 47], the specimens were immersed in 6 wt. %
234 FeCl₃ solution for 20 s at 30 °C to eliminate the pit initiation time prior to immersion
235 experiments according to the ASTM G48-2000 [58]. After the pre-initiated pits, the
236 specimens were ultrasonically cleaned in acetone for 3 min and dried in cold air. The
237 specimens were fixed to the rotating cage and immediately immersed into the
238 autoclave.

239

240 The heteromorphic electrode was designed to investigate the pit growth at various
241 flow rates [59]. Fig. 3 shows the flow distribution at the surface of the heteromorphic
242 electrode, whereas the corresponding results are presented in Table 3. When the flow

243 rate of the marked surface 6 was controlled at 1 m/s, the marked surfaces 1, 2, and 5
244 experienced the flow rates of 0.31 m/s, 0.5 m/s and 0.72 m/s, respectively. The
245 bump-shaped specimens were evenly arranged around the central axis of the rotating
246 cage and mounted within the autoclave.

247

248 A schematic of the corrosion rotating cage with various stress levels is displayed in
249 [Fig. 4](#). The calculated tensile stress distribution is shown in [Fig. 5\(a\)](#). The finite
250 element analysis results showed that various tensile stresses for different width
251 sections could be achieved. For the Surface-3, the tensile stress was fixed at 350 MPa,
252 whereas the tensile stresses of 210 MPa, 175 MPa and 270MPa were set for
253 Surfaces-1, -2, and -4, respectively. In addition, the tensile stress and flow rate
254 distribution of T-type flat specimen are shown in [Figs. 5\(b\)](#) and [5\(c\)](#). The constant
255 tensile stress area exhibited a stable flow rate, which indicated that the T-type sample
256 and the stress corrosion rotating cage could be used to simulate the stress, flow rate
257 and the coupling experiments.

258

259 According to the experimental design presented in [Table 4](#), the immersion
260 experiments were performed at various temperatures/CO₂ pressures, flow rates, and
261 stresses using the stress corrosion rotating cage with T-type tensile stress specimens
262 for 30 days. Four independent specimens were used to measure the maximum pitting
263 depth in each experiment.

264

265 After the experiments, the specimens were ultrasonically cleaned in acetone for 5 min.
266 Then, the specimens were dried using cold air and stored in a desiccator before
267 measuring the pit depth. The morphology of the pits was determined using an
268 OLS4100 confocal laser scanning microscope. The maximum pit depth was recorded.
269 Meanwhile, the Gumbel distribution was used to model the behavior of maximum
270 pitting depth. The cumulative probability $F(Y)$ of the maximum pitting depth can be
271 given by Equation (2) [47, 60].

$$272 \quad F(Y) = \exp\{-\exp[-(\frac{D_{max}-\mu}{\lambda})]\} \quad (2)$$

273 where D_{max} represents the maximum pitting depth, μ refers to the central parameter
274 (the most frequent value) and λ denotes the scale parameter. The two parameters μ
275 and λ are calculated from the relationship of reduced variant (Y) and D_{max} , where Y
276 can be calculated using the correlation: $Y = -\ln\{-\ln[F(Y)]\}$.

277

278 **2.6 Field data measurement**

279 The corroded tubing over the past six-years was collected in Tarim. Along the well
280 profile, the maximum pit depth of HP-13Cr SS was monitored using a micrometer pit
281 depth gauge attached to a bridging bar. The tubing was cut into small pieces (50 mm ×
282 50 mm). The specimens were ultrasonically cleaned in acetone for 5 min, and pitting
283 depth was measured using the OLS4100 confocal laser scanning microscope.

284

285 **3. Results and discussion**

286 **3.1 Pit initiation time**

287 According to a previously proposed pit initiation model [47], the schematic of the
288 pitting corrosion is shown in Fig. 6. The t_{init} was related to the applied potential (E_{app}),
289 open circuit potential (E_{ocp}) and the E_{rp} , whereas it was equal to the intersection point
290 of the $E_{\text{app}}-E_{\text{rp}}$ and $E_{\text{ocp}}-E_{\text{rp}}$.

291

292 3.1.1 Determination of E_{rp}

293 As reported in Zhang's group previous work and Sridhar's model, E_{rp} can be regarded
294 as the critical potential to predict the pitting corrosion. The relationship between
295 pitting potential (E_{pit}) [43, 47, 61], E_{rp} and square root of the potential sweep rate ($v^{1/2}$)
296 was obtained through the cyclic potentiodynamic polarization tests. The potential
297 sweep rate was nearly zero throughout the service-life of HP-13Cr SS. Therefore, at
298 zero potential sweep rate, the E_{rp} and E_{pit} of HP-13Cr SS need to be corrected under
299 different temperatures and CO₂ pressures.

300

301 Fig. 7 displays the cyclic potentiodynamic polarization curves for HP-13Cr SS under
302 various temperatures and CO₂ pressures. The curves were drawn under different scan
303 rates and the values of E_{pit} and E_{rp} are summarized in Table 5. Both the E_{pit} and E_{rp}
304 decreased with the increase of scan rate. Meanwhile, E_{pit} and E_{rp} shifted towards the
305 cathodic direction with the increase in temperature and pressure. The minimum values
306 of 152.66 ± 3.13 mV_{SHE} and -212.38 ± 0.78 mV_{SHE} were obtained at 180 °C/3.8 MPa.
307 It can be noted that E_{pit} and E_{rp} linearly increased with the square root of sweep rate
308 ($v^{1/2}$) under various temperatures and CO₂ pressures, as shown in Fig. 8. Meanwhile,

309 the value of E_{pit} and E_{tp} at the sweep rate of 0 mV/s could be predicted [62], as
310 presented in Table 4.

311

312 3.2 Evolution of the OCP

313 The monitored OCP for various immersion times can be used to predict the
314 occurrence of pitting [43]. The OCP evolution with time can be described using
315 Equation (3) [43, 63].

$$316 \quad E = E_{\text{oc}} - \frac{1}{\gamma} \ln \left[\frac{-B\gamma}{A} t + \exp[-\gamma(E_{\text{corr}} - E_{\text{oc}})] \right] \quad (3)$$

317 where γ represents the Tafel constant for the cathodic electrode reaction, E_{oc} refers to
318 the cathodic electrode reaction equilibrium potential, and A and B are the constants
319 and their values are related to the naturally formed passive film.

320 The equation proposed by Burstein et al. (Equations (4)-(5)) [64-65] indicates that the
321 proposed OCP evolution (as given by Equation (3)) considers the nature of passive
322 film formed on stainless steel. Therefore, the Equation (3) allows for extrapolation of
323 passive film formed on HP-13Cr SS under various temperatures and CO₂ pressures.

$$324 \quad E = A_1 \ln t + B_1 \quad (4)$$

$$325 \quad E = E_{\text{oc}} - A_2 - \frac{1}{\gamma} \ln t \quad (5)$$

326 where A_1 and B_1 refer to the fitting parameters, which depend on the pH value, and A_2
327 is a constant. In order to predict the OCP evolution at various temperatures and CO₂
328 pressures, some critical parameters are listed in Table 6. The γ and i_0 can be
329 calculated from the cathodic polarization curves based on the Butler-Volmer equation.
330 Additionally, the values of the electric field strength (ϵ_L), E_{oc} and the Point Defect

331 Model (PDM) parameters were taken from our previous work [14, 47]. Therefore,
332 OCP changes with immersion time under various temperatures and CO₂ pressures, as
333 described by Equations (6)-(9).

334
$$E (\text{mV}_{\text{SHE}}) = -182.7 + 89.36 \times \ln(0.028 \times t + 0.354) \quad (95 \text{ }^\circ\text{C}/ 2.8\text{MPa}) \quad (6)$$

335
$$E (\text{mV}_{\text{SHE}}) = -155.1 + 92.67 \times \ln(0.018 \times t + 0.253) \quad (120 \text{ }^\circ\text{C}/ 3.2\text{MPa}) \quad (7)$$

336
$$E (\text{mV}_{\text{SHE}}) = -117.0 + 97.37 \times \ln(0.01 \times t + 0.135) \quad (150 \text{ }^\circ\text{C}/ 3.6 \text{ MPa}) \quad (8)$$

337
$$E (\text{mV}_{\text{SHE}}) = -72.8 + 91.07 \times \ln(0.072 \times t + 0.051) \quad (180 \text{ }^\circ\text{C}/ 3.8 \text{ MPa}) \quad (9)$$

338 The calculated OCP values are displayed in Fig. 9. The values increase continuously
339 over time, which is consistent with the measured data [66]. The results show that the
340 OCP values exceeded E_{rp} after 38.4 days, 22.2 days, 21.7 days, and 18.1 days under
341 the temperature/pressure of 95 °C/2.8 MPa, 120 °C/3.2MPa, 150 °C/3.6 MPa and
342 180 °C/3.8 MPa, respectively.

343

344 3.3 Pit induction time (t_{ind}) above E_{rp}

345 The relationship between the pit induction time (t_{ind}) and the applied potential (E_{app})
346 can be given by Equation (10) [47].

347
$$t_{\text{ind}} = a \exp(-b \cdot \Delta E) + c \quad (10)$$

348 where a , b , and c are constants, and ΔE represents the difference between E_{app} and
349 $E_{\text{rp}(v=0)}$. Fig. 10 shows the time dependence of current density on a logarithmic scale
350 for HP-13Cr SS immersed in the formation solution at various applied potentials. The
351 turning point in Fig. 10 between the passive stage and the pit growth changed,
352 suggesting that t_{ind} was highly influenced by temperatures and pressures. As shown in
353 Fig. 10, t_{ind} decreased with the increase in the value of ΔE . Fig. 11 indicates that the

354 values of a , b , and c decreased with the increase in temperature and CO₂ pressure.
 355 However, the pit initiation time (t_{init}) cannot be regarded as a simple sum of $t_{OCP \rightarrow E_{rp}}$
 356 and t_{ind} . Based upon our previous work [47], t_{init} can be obtained using Equation (11).

$$357 \quad \begin{cases} E = E_{oc} - \frac{1}{\gamma} \ln \left[\frac{-By}{A} t_{init} + \exp[-\gamma(E_{corr} - E_{oc})] \right] \\ t_{init} = t_{OCP \rightarrow E_{rp}} + a \exp[-b \cdot (E - E_{rp(v=0)})] + c \quad (E > E_{rp}) \end{cases} \quad (11)$$

358
 359 Graphical method is used to calculate the value of t_{init} and the corresponding results
 360 under different temperatures and pressures are presented in Fig. 12. With the increase
 361 in temperature and pressure from 95 °C/2.8 MPa to 180 °C/3.8 MPa, the t_{init} values
 362 were 76.8 days, 39.7 days, 34.6 days, and 28.6 days, respectively. In addition, several
 363 researchers concluded that the flow rate and stress played a significant role in
 364 accelerating the t_{init} [11-30]. Moreover, the maximum t_{init} was far shorter than the
 365 required design service life-time (15 years) for HP-13Cr SS under the current
 366 conditions. The critical factor determining the life-time was the pitting growth process.
 367 Herein, the correction of t_{init} by the flow rate and stress could be neglected. Based
 368 upon Fig. 1, the temperature and CO₂ pressure increased with the depth of the well.
 369 Therefore, the relationship between t_{init} and temperature/CO₂ pressure can be
 370 transformed into t_{init} and the depth of well. The results are shown in Fig. 13, whereas
 371 nonlinear fitting equation is given by Equation (12).

$$372 \quad t_{init} = 30.20 + 130.61 \times \exp(-1.29 \times Depth(km)) \quad (12)$$

373

374 **3.2 Mechanistic model for the single factor**

375 For HP-13Cr SS, t_{init} of 76.8 days was obtained for 95 °C/2.8 MPa, which is too long

376 to investigate the pit growth. In the present work, the pre-initiated pits on HP-13Cr SS
377 were used to study the pit initiation time. The cumulative probability plot and the
378 Gumbel plot of the maximum pit depth were drawn from 20 specimens after
379 pre-initiated pits, as shown in Fig. 14. The fitted Gumbel distribution (red in Fig. 14)
380 was fairly consistent with the experimentally measured maximum pit depth. The
381 location parameter (μ) and the scale parameter (λ) were found to be 8.28 μm and 0.97,
382 respectively. Moreover, the typical morphologies of the pits after pre-initiation are
383 shown in Fig. 15. The growth of pit after pre-initiated pits on HP-13Cr SS can be
384 described using Equation (13) [47].

$$385 \quad D_{\max} = K[t + (t_0 + t_{\text{init}}) - t_{\text{init}}]^{\omega} = K(t + t_0)^{\omega} \quad (13)$$

386 where t_0 refers to the pit growth time. Furthermore, the mechanistic model for pit
387 growth under various temperatures, CO₂ pressures, flow rates, and stress levels will
388 be discussed in detail in the following paragraphs. The morphologies of the maximum
389 pit and the Gumbel plots under various condition are shown in Appendix 1.

390

391 **3.2.1 Mechanistic model for temperature/CO₂ pressure**

392 Fig. 16 shows the Gumbel plots of the maximum pit depths measured for ten
393 specimens at various temperatures and CO₂ pressures. It is worth noticing that the
394 fitted Gumbel distribution shifted to the right and rotated clockwise with the increase
395 in immersion time, which is in good agreement with the previously reported data [67].

396 In addition, the local parameter (μ) and scale parameter (λ) are presented in Table 7.

397 Moreover, the time-dependence of the averaged maximum pit depth under various

398 temperatures and CO₂ pressures is presented in Fig 17. The variation of the averaged
 399 maximum pit depth with time can be fitted using Equation (12). With the increase in
 400 temperatures and CO₂ pressures, the pit proportionality (K) increased from 4.53 to
 401 13.46, whereas the pitting exponent (ω) increased from 0.417 to 0.487 (following Eq.
 402 14). Therefore, the results revealed that the growth rate of pit increased with the
 403 increase in temperature and CO₂ pressure. Moreover, one should notice that ω was
 404 located within the range of 0.417 - 0.487. When the ω was about 0.5, the pit growth
 405 was controlled by diffusion [68]. The depth of pits increased with the increase in
 406 temperature and CO₂ pressure, while the typical pit morphologies are shown in Fig.
 407 S1 (Appendix 1). In addition, the relationship between the pit growth parameters and
 408 the well depth are provided in Fig. 18.

$$409 \quad \begin{cases} K = 4.46 + 0.26 \times \exp(0.44 \times depth) \\ \omega = 0.37 + 0.05 \times \exp(0.12 \times depth) \end{cases} \quad (14)$$

410 The maximum pit depth can be calculated using Equation (15).

$$411 \quad D_{\max} = [4.46 + 0.26 \times \exp(0.44 \times depth)] \times t^{0.37+0.05 \times \exp(0.12 \times depth)} \quad (15)$$

412

413 3.2.2 Effect of the flow rate on the mechanistic model

414 As shown in Fig. S2 (Appendix 1), the Gumbel distribution describes the maximum
 415 pit depth under various flow rates. Fig. 19 shows the development of averaged
 416 maximum pit depth, which was fitted from the Gumbel plots (as displayed in Table S1
 417 (Appendix 1)). It can be seen that the maximum pit depth gradually decreased with
 418 the increase in flow rate within the range of 0.31-1 m/s. Furthermore, the growth
 419 kinetics of pits was fitted using Equation (10), and the results show that the value of K

420 decreased from 4.86 to 3.70 when the flow rate increased from 0.31 m/s to 1 m/s. The
 421 decrease in growth rate of the pit was mainly attributed to the vortex generated inside
 422 the pit, where the distribution of H⁺ and metal ion was inhomogeneous [15]. The pit
 423 morphologies are displayed in Fig. S3 (Appendix 1), indicating that the presence of
 424 vortex accelerated the pit growth in the horizontal direction and formed the
 425 shallow-disk shape pit on the surface of HP-13Cr SS.

426 Fig. 20 exhibits the relationship between K and flow rate (V) using Equation (16).

$$427 \quad K = -2.93 \times \exp(0.43 \times V) + 8.15 \quad (16)$$

428 Then, the D_{\max} for the flow rate can be described using Equation (17).

$$429 \quad D_{\max} = [-2.93 \times \exp(0.43 \times V) + 8.15] \times t^{0.42} \quad (17)$$

430

431 3.2.3 Effect of stress on the growth of pit

432 Based upon the results presented in Fig. 1, it can be noted that there was a transition
 433 between the tensile stress and the compressive stress along the well's depth. The stress
 434 distribution can be calculated based on the pipe mechanics using Equation (18).

$$435 \quad \begin{cases} F = -0.088d + 425.93 & (\text{tensile stress, } d \leq 5000m) \\ F = -0.088d + 425.93 & (\text{compress stress, } 5000m \leq d \leq 7500m) \\ F = -0.078d + 624 & (\text{tensile stress, } 7500m \leq d \leq 8000m) \end{cases} \quad (18)$$

436 The tensile stress and the compressive stress accompany a positive and a negative
 437 sign, respectively.

438

439 Fig. 21(a) indicates that the maximum pit depth increased significantly with the
 440 increase in tensile stress due to the mechanical-electrochemical effect, which is
 441 consistent with some previous studies [30-31]. The relationship among K , ω and

442 stress can be expressed using Equations (19) and (20).

$$443 \quad K = \begin{cases} 0.016 \times \exp(-0.012 \times F) + 5.47 & \text{(tensile stress)} \\ -0.09 \times \exp(-0.0056 \times F) + 5.40 & \text{(compression stress)} \end{cases} \quad (19)$$

$$444 \quad \omega = \begin{cases} 0.041 \times \exp(0.0026 \times F) + 0.40 & \text{(tensile stress)} \\ 0.44 & \text{(compression stress)} \end{cases} \quad (20)$$

445

446 The pit morphologies are displayed in Fig. S5 (Appendix 1) and suggested that a large
447 pit was formed on the surface under the effect of tensile stress. However, the increase
448 in compressive stress within the range of 0-250 MPa represented a limited effect on
449 the growth rate of a pit, as shown in Fig. 21(b). The values of K and ω with respect
450 to the stress are presented in Fig 22. It can be noticed that the turning point appeared
451 at $F = 0$ MPa (Fig 22(a)). However, the differences between the compressive and
452 tensile stress values in terms of ω values can be neglected. For the compressive
453 stress, ω remained around 0.44, whereas ω gradually increased from 0.453 to 0.493
454 as the tensile stress increased from 175 MPa to 350 MPa. Therefore, the D_{\max} value
455 under the impact of stress bounced back following Equation (13), and the relationship
456 can be expressed using Equations (21) and (22).

457

458 For tensile stress (0 - 350 MPa):

$$459 \quad D_{\max} = [0.016 \times \exp(-0.012 \times F) + 5.47] \times t^{0.041 \times \exp(0.0026 \times F) + 0.40} \quad (21)$$

460 For compressive stress (0 - -250 MPa):

$$461 \quad D_{\max} = [-0.09 \times \exp(-0.0056 \times F) + 5.40] \times t^{0.44} \quad (22)$$

462

463 **3.3 Multi-degree of freedom model for predicting pitting damage under complex**

464 **oilfield environment**

465 The mechanistic-chemometrics model proposed in this work can be divided into two
466 processes: (i) the mechanistic-model under different factors, (ii) Combining the single
467 factor mechanistic-model using the weight coefficients of each factor and their mutual
468 interactions. A combination of weight coefficients and sub-model to formulate the pit
469 prediction model can be described using Equation (23).

470
$$D_{\max} = \sum_i f_i K_i (t - t_{\text{init}})^{\omega_i} \quad (23)$$

471 where i refers the influencing factors, and includes temperature, CO₂ pressure, flow
472 rate, stress and interaction of each factor with others. Moreover, f_i represents the
473 weight coefficient of i^{th} factor, and K_i and ω_i represent the pit proportionality and
474 exponent of i^{th} factor, respectively.

475

476 **3.3.1 Determination of the weight coefficient using chemometrics method**

477 **Table 2** summarizes the designed experiments and presents the measured maximum
478 pit depth on the surface of HP-13Cr SS after being immersed in CO₂-saturated
479 formation water for 30 days. The pit morphologies are displayed in **Fig. S8 (Appendix**
480 **1)**. The relationship between the maximum pit depth and the influencing factors using
481 the statistical regression analysis can be given by Equation (24).

482
$$D_{\max} = 13.09 + 6.52x_1 - 0.80x_2 + 3.50x_3$$

483
$$-0.54x_1x_2 + 2.39x_1x_3 - 0.18x_2x_3$$

484
$$-0.076x_1x_2x_3$$

485 (24)

486 where x_1 , x_2 , and x_3 represent the influencing factors (temperature/pressure,
487 flow rate, and stress, respectively), and $x_i x_j$ (i and $j = 1, 2, 3$) represents the
488 interaction terms. Moreover, the influence of various factors and the interactions
489 on the maximum pit depth were further justified using the ANOVA analysis.

490 As shown in Fig. 23, temperature/CO₂ pressure is the most significant factor,
491 followed by the stress and the combined influence of temperature/CO₂ pressure
492 and stress. The effect of a given factor became significant if its F -value was
493 higher than the critical value of 11.26. The flow rate and interactions among
494 factors were not significant for the pitting corrosion in the complex oil field
495 environment. The regression model can be simplified as Equation (25).

$$496 \quad D_{max} = 13.09 + 6.52x_1 + 3.50x_3 + 2.39x_1x_3 \quad (25)$$

497 The Pareto analysis is proposed as a quantitative method to determine the weight
498 coefficients of the maximum pit depth, as given by Equation (26) [50].

$$499 \quad P_i = \left(\frac{a_i^2}{\sum_{i \neq 0} a_i^2} \right) \times 100\% \quad (26)$$

500 where P_i refers to the percentage effect of each variable on pit depth and a_i represents
501 the coefficient of each variable. The results of Pareto analysis are shown in Fig. 23. It
502 can be noted that the temperature/pressure are the most significant factors, followed
503 by stress, and stress interaction, with the corresponding weight coefficients of 52.54%,
504 28.20%, and 19.26%, respectively.

505

506 3.3.2 Validation of the model with field data

507 Based on Equation (22), the mechanistic-chemometrics model can be described as

508 Equation (27).

509

$$510 \quad \begin{cases} t_{\text{ind}} = 52.54\% \times t_{T/P} - 28.20\% \times t_F - 19.26\% \times (t_{T/P} \times t_F) \\ K = 52.54\% \times K_{T/P} + 28.20\% \times K_F + 19.26\% \times (K_{T/P} \times K_F) \\ \omega = 52.54\% \times \omega_{T/P} + 28.20\% \times \omega_F + 19.26\% \times (\omega_{T/P} \times \omega_F) \end{cases} \quad (27)$$

511

512 The maximum pit depths are summarized in Table 2. Valor et al. [65], Provan et al.
513 [69], and Cavanaugh et al. [70] reported that the growth kinetics of pits can be
514 simplified as $D_{\text{max}} = Kt^\omega$, when the t_{init} is small compared to the immersion time,
515 and suggested that the t_{init} can be neglected in predicting the long-term pit damage for
516 HP-13Cr SS under complex oilfield environment.

517

518 In order to verify the accuracy of the model for a complex oil environment, the
519 maximum pit depth formed on HP-13Cr SS was measured after 6 years in service.
520 The maximum pit depth along the depth of the well is displayed in Fig. 24. It can be
521 seen clearly that the pit depth initially decreased with the increase in the depth of the
522 well, followed by a sharp increase. The results also indicate that the maximum pit
523 depths were found near the top and bottom of the well. As a comparison, the predicted
524 maximum pit depth along the well profile is shown in Fig. 24. The proposed
525 mechanistic-chemometrics model is highly reliable in predicting the pitting damage
526 and can be utilized in current oilfield environments.

527

528 **4. Conclusions**

529 The multi-degree of freedom model has been developed to predict the pit behavior
530 under complex oilfield environment using a combination of weight coefficients and
531 sub-models of temperature/pressure, flow rate and stress. Based upon the results,
532 following conclusions are drawn.

533

534 (1) The t_{init} value decreased with the increase in temperature/CO₂ pressure, and the
535 correction of t_{init} by flow rate and stress could be neglected. Finally, the
536 relationship between t_{init} and temperature/CO₂ pressure can be applied to the
537 whole depth of the well.

538

539 (2) The growth rate of a pit is accelerated with the increase in temperature/CO₂
540 pressure, flow rate and tensile stress. Moreover, the compressive stress shows a
541 negligible effect on the growth of pit.

542

543 (3) For a chemometrics method, two-level factorial design is performed to identify the
544 most significant factors and interactions influencing the pit depth formed on the
545 HP-13Cr SS surface under complex oilfield environments. The temperature/CO₂
546 pressure, stress and their interactions were identified as the most significant factors
547 in terms of pit depth, and the weight coefficients were determined to be 52.54%,
548 28.20% and 19.26%, respectively.

549

550 (4) The measured data from Tarim area. in China confirmed the reliability of the

551 proposed model for predicting the pitting behavior of HP-13Cr SS oil tubes under
552 complex oilfield environment.

553

554 **Data availability**

555 The raw/processed data required to reproduce these findings cannot be shared at this
556 time, as the data form part of another ongoing study.

557

558 **Authorship contribution statement**

559 **Yang Zhao**: Investigation, Writing - original draft. **Yong Hua**: Investigation,
560 Visualization, Writing - review and editing. **Bin Liu**: Investigation, Funding
561 acquisition. **Xuanpeng Li**: Conceptualization, Writing - review and editing, Funding
562 acquisition. **Junfeng Xie**: Writing - review and editing. **Guanxin Zeng**: Writing -
563 review and editing. **Tao Zhang**: Conceptualization, Writing - review and editing,
564 Funding acquisition. **Fuhui Wang**: Writing - review and editing.

565

566 **Acknowledgements**

567 The authors wish to acknowledge the financial support provided by the National Key
568 Research and Development Program of China (Grant No.: 2017YFB0702203), the
569 National Natural Science Foundation of China (Grant No. U1460202), the National
570 program for the Young Top-notch Professionals, the Fundamental Research Funds for
571 the Central Universities (Grant No.: N170205002) and the Key Laboratory of
572 Superlight Material and Surface Technology (Harbin Engineering University, China),

573 Ministry of Education, China and the Chinese Postdoctoral Science Foundation
574 (Grant No.: 01270012810066).

575

576 **References**

577 [1] H. Pang, J.Q. Chen, X.Q. Pang, L.F. Liu, K.Y. Liu, C.F. Xiang, Key factors
578 controlling hydrocarbon accumulations in Ordovician carbonate reservoirs in the
579 Tazhong area, Tarim basin, western China, *Mar. Petrol. Geol.* 43 (2013) 88 - 101.

580 [2] P. Li, Y Zhao, B. Liu, G.X. Zeng, T. Zhang, D.K. Xu, H. Gu, T.Y Gu, F.H. Wang,
581 Experimental testing and numerical simulation to analyze the corrosion failures of
582 single well pipelines in Tahe oilfield, *Eng. Fail. Anal.* 80 (2017) 112 - 122.

583 [3] C.I. Ossai, B. Boswell, I.J. Davies, Pipeline failures in corrosive environments - a
584 conceptual analysis of trends and effects, *Eng. Fail. Anal.* 53 (2015) 36 - 58.

585 [4] Y. Zhao, W.L Qi, J.F. Xie, Y. Chen, T. Zhang, D.K. Xu, F.H. Wang, Investigation
586 of the failure mechanism of the TG-201 inhibitor: Promoting the synergistic effect of
587 HP-13Cr stainless steel during the well completion, *Corros. Sci.* 166 (2020) 108448.

588 [5] X.T. Yang, X.P. Shen, X.H. Cui, K.L. Wang, G.Y. Shen, Z.B. Wang, T. Qin, Stress
589 and deformation characteristics of completion and testing tubing string with
590 expansion joints for ultra-deep HTHP gas wells, *Natural. Gas. Industry. B.* 7 (2020)
591 101-108.

592 [6] X. Yue, L. Zhang, Y. Wang, S. Xu, C. Wang, M. Lu, A. Neville, Y. Hua, Evolution
593 and characterization of the film formed on super 13Cr stainless steel in CO₂-saturated
594 formation water at high temperature, *Corros. Sci.* 163 (2020) 108277.

- 595 [7] X.W. Lei, Y.R. Feng, A.Q. Fu, J.X. Zhang, Z.Q. Bai, C.X. Xin, C.H. Lu,
596 Investigation of stress corrosion cracking behavior of super 13Cr tubing by full-scale
597 tubular goods corrosion test system, *Eng. Fail. Anal.* 50 (2015) 62-70.
- 598 [8] Y. Zhao, J. Xie, G. Zeng, T. Zhang, D. Xu, F. Wang, Pourbaix diagram for
599 HP-13Cr stainless steel in the aggressive oilfield environment characterized by high
600 temperature, high CO₂ partial pressure and high salinity, *Electrochim. Acta.* 293 (2019)
601 116 – 127.
- 602 [9] R.M. Moreira, C.V. Franco, C.J.B.M. Joia, S. Giordana, O.R. Mattos, The effects
603 of temperature and hydrodynamics on the CO₂ corrosion of 13Cr and 13Cr5Ni2Mo
604 stainless steels in the presence of free acetic acid, *Corros. Sci.* 46 (2004) 2987 - 3003.
- 605 [10] T. Sunaba, T. Ito, Y. Miyata, S. Asakura, T. Shinohara, T. Yakou, Y. Tomoe, H.
606 Honda, Influence of chloride ions on corrosion of modified martensitic stainless steels
607 at high temperatures under a CO₂ environment, *Corrosion.* 70 (2014) 988 - 999.
- 608 [11] S. Nestic, Key issues related to modelling of internal corrosion of oil and gas
609 pipelines - A review, *Corros. Sci.* 49 (2007) 4308 - 4338.
- 610 [12] L.J. Mu, W.Z. Zhao, Investigation on carbon dioxide corrosion behaviour of
611 HP13Cr110 stainless steel in simulated stratum water, *Corros. Sci.* 52 (2010) 82-89.
- 612 [13] H. Zhang, Y. L. Zhao, Z. D. Jiang, Effects of temperature on the corrosion
613 behavior of 13Cr martensitic stainless steel during exposure to CO₂ and Cl⁻
614 environment, *Mater. Lett.* 59 (2005) 3370-3374.
- 615 [14] X.P. Li, Y. Zhao, W.L. Qi, J.D. Wang, B. Liu, G.X. Zeng, T. Zhang, F.H. Wang,
616 Effect of extremely aggressive environment on the nature of corrosion scales of

617 HP-13Cr stainless steel, *Appl. Sur. Sci.* 469 (2019) 146 -161.

618 [15] Y. Zhao, X. Li, C. Zhang, T. Zhang, J. Xie, G. Zeng, D. Xu, F. Wang,
619 Investigation of the rotation speed on corrosion behavior of HP-13Cr stainless steel in
620 the extremely aggressive oilfield environment by using the rotating cage test, *Corros.*
621 *Sci.* 145 (2018) 307–319.

622 [16] S Nesic, Effects of multiphase flow on internal CO₂ corrosion of mild steel
623 pipelines, *Energ. Fuel.* 26 (2012) 4098-4111.

624 [17] G. Schmitt, M. Mueller, Critical Wall Shear Stresses in CO₂ Corrosion of Carbon
625 Steel, *Corrosion/1999*, NACE International, Houston/TX, 1999 paper no. 44.

626 [18] L.N. Xu, S.Q. Guo, W. Chang, T.H. Chen, L.H. Hu, M.X. Lu, Corrosion of Cr
627 bearing low alloy pipeline steel in CO₂ environment at static and flowing conditions,
628 *Appl. Surf. Sci.* 270 (2013) 395-404.

629 [19] J.A. Wharton, R.J.K. Wood, Influence of flow conditions on the corrosion of
630 AISI 304L stainless steel, *Wear.* 256 (2004) 525–536.

631 [20] L. Wei, X.L. Pang, K.W. Gao, Effect of flow rate on localized corrosion of X70
632 steel in supercritical CO₂ environments, *Corros. Sci.* 136 (2018) 339–351.

633 [21] X.Z. Wang, H. Luo, J.L. Luo, Effects of hydrogen and stress on the
634 electrochemical and passivation behaviour of 304 stainless steel in simulated PEMFC
635 environment, *Corros. Sci.* 145 (2018) 307–319.

636 [22] D. Chastell, P. Doig, P.E.J. Flewitt, K. Ryan, The influence of stress on the pitting
637 susceptibility of a 12%CrMoV martensitic stainless steel, *Corros. Sci.* 19 (1979)
638 335-341.

639 [23] S.J. Lennon, F.P.A. Robinson, G.G. Garrett, The influence of applied stress and
640 surface finish on the pitting susceptibility of low alloy turbine disk steels in wet steam,
641 *Corrosion*. 40 (1984) 409-413.

642 [24] G. Vanboven, W. Chen, R Rogge, The role of residual stress in neutral pH stress
643 corrosion cracking of pipeline steels. Part I: Pitting and cracking occurrence, *Acta*
644 *Materialia* 55 (2007) 29-42.

645 [25] A. Turnbull, L.N. McCartney, S. Zhou, A model to predict the evolution of pitting
646 corrosion and the pit-to-crack transition incorporating statistically distributed input
647 parameters, *Corros. Sci.* 48 (2006) 2084–2105.

648 [26] H. Iwanaga, T. Oki, Effect of applied stress on anodic polarization behavior and
649 pitting corrosion of stainless steel, *J. Soc. Mater. Sci. Jpn.* 30 (1981) 394-400.

650 [27] V. Vignal, N. Mary, R. Oltra, J. Peultier, A mechanical-electrochemical approach
651 for the determination of precursor sites for pitting corrosion at the microscale, *J.*
652 *Electrochem. Soc.* 153 (2006) B352-B357.

653 [28] X. Feng, Y. Zuo, Y. Tang, X. Zhao, X. Lu, The degradation of passive film on
654 carbon steel in concrete pore solution under compressive and tensile stresses,
655 *Electrochim. Acta.* 58 (2011) 258-263.

656 [29] S. Guo, H.T. Wang, E.H. Han, Computational evaluation of the influence of
657 various uniaxial load levels on pit growth of stainless steel under
658 mechanochemical interactions, *J. Electrochem. Soc.* 165 (2018) C515-C523.

659 [30] O. O. Fatoba, R. Leiva-Garcia, S.V. Lishchuk, N.O. Larrosa, R. Akid, Simulation
660 of stress-assisted localised corrosion using a cellular automaton finite element

661 approach, Corros. Sci. 137 (2018) 83-97.

662 [31] E.M. Gutman, Mechanochemistry of solid surface, World Scientific Publishing
663 Company, Singapore (1994).

664 [32] R. Elgaddafi, R. Ahmed, S. Shah, Corrosion of carbon steel in CO₂ saturated
665 brine at elevated temperatures, J. Petrol. Sci. Eng.196 (2021) 107638.

666 [33] Y. Hua, S. Xu, Y. Wang, W. Taleb, J. Sun, L. Zhang, R. Barker, A. Nevillea, The
667 formation of FeCO₃ and Fe₃O₄ on carbon steel and their protective capabilities against
668 CO₂ corrosion at elevated temperature and pressure, Corros. Sci. 157 (2019) 392-405.

669 [34] A. Dugstad, L. Lunde, K. Videm, Parametric study of CO₂ corrosion of carbon
670 steel, Corrosion/94, paper no. 14 (Houston, TX: NACE International, 1994).

671 [35] C. de Waard, U. Lotz, A. Dugstad, Influence of liquid flow velocity on CO₂
672 corrosion a semi-empirical model, Corrosion/95, paper no. 128 (Houston, TX: NACE
673 International, 1995).

674 [36] C. de Waard, U. Lotz, Prediction of CO₂ corrosion of carbon steel, Corrosion/93,
675 paper no. 69 (Houston, TX: NACE International, 1993).

676 [37] A. Ikeda, S. Mukai, M. Ueda, Prevention of CO₂ corrosion of line pipe and oil
677 country tubular goods, Corrosion/84, paper no. 289 (Houston, TX: NACE
678 International, 1984).

679 [38] C. de Waard, L. Smith, B.D. Craig, The influent of crude oil on well tubing
680 corrosion rates, EUROCORR, 2001.

681 [39] S. Nestic, J. Postlethwaite, S. Olsen, An electrochemical model for prediction of
682 CO₂ Corrosion, Corrosion/ 95, paper no. 131 (Houston, TX: NACE International,

683 1995).

684 [40] S. Nestic, M. Nordsveen, R. Nyborg, A. Stangeland, A mechanistic model for CO₂
685 corrosion of mild steel in the presence of protective iron carbonate scales – Part II: A
686 numerical experiment, *Corrosion*. 59 (2003) 489.

687 [41] A. Kahyarian, M. Singer, S. Nestic, Modeling of uniform CO₂ corrosion of mild
688 steel in gas transportation systems: A review, *J. Nat. Gas. Sci. Eng.* 29 (2016)
689 530-549.

690 [42] A. Valor, F. Caleyó, L. Alfonso, D. Rivas, J.M. Hallen, Stochastic modeling of
691 pitting corrosion: a new model for initiation and growth of multiple corrosion pits,
692 *Corros. Sci.* 49 (2007) 559-579.

693 [43] A. Anderko, N. Sridhar, D. S. Dunn, A general model for the repassivation
694 potential as a function of multiple aqueous solution species, *Corros. Sci.* 46 (2004)
695 1583-1612.

696 [44] G. Engelhardt, D. D. Macdonald, Unification of the deterministic and statistical
697 approaches for predicting localized corrosion damage. I. Theoretical foundation,
698 *Corros. Sci.* 46 (2004) 2755-2780.

699 [45] J.C. Velázquez, F. Caleyó, A. Valor, J.M. Hallen, Predictive model for pitting
700 corrosion in buried oil and gas pipelines. *Corrosion*. 65 (2009) 332-342.

701 [46] H. Qin, W. Zhou, S. Zhang, Bayesian inferences of generation and growth of
702 corrosion defects on energy pipelines based on imperfect inspection data. *Reliab. Eng.*
703 *Syst. Safe.* 144 (2015) 334-342.

704 [47] X. Li, Y. Zhao, W. Qi, J. Wang, J. Xie, H. Wang, L. Chang, B. Liu, G. Zeng, Q.

705 Gao, H. Sun, T. Zhang, F.H. Wang, Modeling of pitting corrosion damage based on
706 electrochemical and statistical methods, *J. Electrochem. Soc.* 166 (2019) C539-C549.

707 [48] R. Sánchez-Tovar, M.T. Montañés, J. García-Antón, Contribution of the flowing
708 conditions to the galvanic corrosion of the copper/AISI 316L coupling in highly
709 concentrated LiBr solutions, *Corros. Sci.* 68 (2013) 91-100.

710 [49] J. Liu, T. Zhang, W. Zhang, Y.G. Yang, Y.W. Shao, G.Z. Meng, F.H. Wang,
711 Quantitative modeling for corrosion behavior in complex coupled environment by
712 response surface methodology, *Acta. Metal. Sin-Engl.* 28 (2015) 994-1001.

713 [50] Q.F. Hu, Y.C. Liu, T. Zhang, S.J. Geng, F.H. Wang, Modeling the corrosion
714 behavior of Ni-Cr-Mo-V high strength steel in the simulated deep sea environments
715 using design of experiment and artificial neural network, *J. Mater. Sci. Technol.* 35
716 (2019) 168–175.

717 [51] D. Nakhaie, A. Kosari, J. Mol, E. Asselin, Corrosion resistance of hot-dip
718 galvanized steel in simulated soil solution: A factorial design and pit chemistry study,
719 *Corros. Sci.* 164 (2020) 108310.

720 [52] W. Li, B.F.M. Pots, X. Zhong, S. Nestic, Inhibition of CO₂ corrosion of mild steel
721 - Study of mechanical effects of highly turbulent disturbed flow, *Corros. Sci.* 126
722 (2017) 208-226.

723 [53] Y. Zhao, S.Y. Cao, T. Zhang, J.F. Xie, D.K. Xu, F.H. Wang, A new
724 high-efficiency experimental design for optimizing various flow velocities testing in
725 extremely aggressive formation water, *Acta. Metall. Sin. Engl.* 32 (2019) 944-950.

726 [54] L.Y. Xu, Y.F. Cheng, An experimental investigation of corrosion of X100

727 pipeline steel under uniaxial elastic stress in a near-neutral pH solution, *Corros. Sci.*
728 59 (2012) 103–109.

729 [55] P.J.W. Mark, J. Anderson, *RSM Simplified: Optimizing processes using response*
730 *surface methods for design of experiments*, second edi, CRC Press, [Place of
731 publication not identified], 2017

732 [56] D.D. Macdonald, A.C. Scott, P. Wentreck, External reference electrodes for use
733 in high-temperature aqueous systems, *J. Electrochem. Soc.* 126 (1979) 908-911.

734 [57] ASTM G61-86. Standard Test method for conducting cyclic potentiodynamic
735 polarization measurements for localized corrosion susceptibility of iron-, nickel-, or
736 cobalt-based alloys. 2009.

737 [58] Standard ASTM G-48, Pitting and crevice corrosion resistance of stainless steel
738 and related alloys by the use of ferric chloride solution, method A, in *Annual Book of*
739 *ASTM Standards*, vol. 03.02 (West Conshohocken, PA: ASTM, 1992).

740 [59] ASTM G46-94 (2013) Standard guide for examination and evaluation of pitting
741 corrosion, in *Annual Book of ASTM Standards*, vol. 03.02 (West Conshohocken, PA:
742 ASTM, 2013).

743 [60] T. Zhang, X. L. Liu, Y. W. Shao, G. Z. Meng, F. H. Wang, Corrosion of pure
744 magnesium under thin electrolyte layers, *Electrochim. Acta.* 53 (2008), 7921-7931.

745 [61] D. D. Macdonald, D. F. Heaney, Effect of variable intensity ultraviolet radiation
746 on passivity breakdown of AISI Type 304 stainless steel, *Corros. Sci.*, 42, 1779
747 (2000).

748 [62] A. Anderko, N. Sridhar, M. A. Jakab. A general model for the repassivation

749 potential as a function of multiple aqueous species. 2. Effect of oxyanions on
750 localized corrosion of Fe–Ni–Cr–Mo–W–N alloys [J]. *Corros. Sci.* 50 (2008)
751 3629-3647.

752 [63] K. J. Evans, N. Sridhar, B. C. Rollins, S. Chawla, J. A. Beavers, J. Page,
753 Long-term evolution of corrosion potential of carbon steel in alkaline radioactive
754 waste environments, *Corrosion*. 75 (2018) 106-119.

755 [64] G. T. Burstein, R. J. Cinderey, Evolution of the corrosion potential of
756 repassivating aluminium surfaces, *Corros. Sci.* 33 (1992) 475.

757 [65] R. J. Cinderey, G. T. Burstein, The effects of chromate on the transient
758 repassivation potential of aluminium in chloride solution, *Corros. Sci.* 33 (1992) 493-
759 498.

760 [66] Y. Zhang, M.U. Macdonald, G.R. Engelhardt. Development of localized
761 corrosion damage on low pressure turbine disks and blades. III: application of damage
762 function analysis to the prediction of damage, *Electrochim. Acta.* 69 (2012) 19-29.

763 [67] A. Valor, F. Caleyó, D. Rivas, J. M. Hallena, Stochastic approach to
764 pitting-corrosion-extreme modeling in low-carbon steel, *Corros. Sci.* 52 (2010)
765 910-915.

766 [68] F.A. Almuaili, S.A. McDonald, P.J. Withers, A.B. Cook, D.L. Engelberg,
767 Strain-induced reactivation of corrosion pits in austenitic stainless steel, *Corros. Sci.*
768 125 (2017) 12-19.

769 [69] J.W. Provan, E.S. Rodriguez III, Part I: Development of a Markov description of
770 pitting corrosion, *Corrosion*. 45(1989) 178-192.

771 [70] M.K. Cavanaugh, R.G. Buchheit, N. Birbilis. Modeling the environmental

772 dependence of pit growth using neural network approaches, Corros. Sci. 52 (2010)
773 3070-3077.

774

775

776 **List of figures**

777 Fig.1 Schematic diagram of complex oilfield environment

778

779 Fig. 2 Dimensions of the testing specimens: (a) Electrochemical and immersion
780 testing specimen, (b) bump-shaped electrode, (c) high throughout tensile stress
781 specimen, (d) compress stress specimen, (e) T-type specimen

782

783 Fig. 3 Flow rates distribution of the bump-shaped specimen

784

785 Fig. 4 (a) Schematic diagrams of stress corrosion rotating cage, and (b) specimen
786 assemble

787

788 Fig. 5 (a) and (b) von Mises stress distribution of the flat high throughout tensile
789 stress specimen and the T-type specimen, (c) flow distribution around the T-type
790 specimen

791

792 Fig. 6 Schematic of pitting corrosion processes to construct the pitting damage
793 prediction model

794

795 Fig. 7 Cyclic potentiodynamic polarization curves of HP-13Cr SS in simulation
796 formation water at different potential scan rates under various temperatures and CO₂
797 pressures: (a) 95 °C / 2.8 MPa, (b) 120 °C / 3.2 MPa, (c) 150 °C / 3.6 MPa, (d) 180 °C /
798 3.8 MPa

799

800 Fig. 8 E_{pit} (a) and E_{rp} (b) at different potential scan rates (v) for HP-13Cr SS in
801 formation water at different temperatures and CO₂ pressures

802

803 Fig. 9 OCP evolution of HP-13Cr SS in formation water under various temperatures
804 and CO₂ pressures

805

806 Fig.10 Variation of current density (i) with stable pit formation time of HP-13Cr SS in
807 formation water under various temperatures and CO₂ pressures: (a) 95 °C / 2.8 MPa,
808 (b) 120 °C / 3.2 MPa, (c) 150 °C / 3.6 MPa, (d) 180 °C / 3.8 MPa

809

810 Fig. 11 Variation of pit induction time with ΔE ($E_{\text{app}} - E_{\text{rp}}$) of HP-13Cr SS under
811 various temperatures and CO₂ pressures: (a) 95 °C / 2.8 MPa, (b) 120 °C / 3.2 MPa, (c)
812 150 °C / 3.6 MPa, (d) 180 °C / 3.8 MPa

813

814 Fig.12 Pit initiation time of HP-13Cr SS in formation water under various
815 temperatures and CO₂ pressures: (a) 95 °C / 2.8 MPa, (b) 120 °C / 3.2 MPa, (c) 150 °C

816 / 3.6 MPa, (d) 180 °C / 3.8 MPa

817

818 Fig.13 Variety of pit initiation time of HP-13Cr SS in formation water with well depth

819

820 Fig. 14 Cumulative probability and Gumbel plot of maximum pit depth for HP-13Cr

821 SS after pre-initiated pits

822

823 Fig. 15 Typical morphologies of maximum pits for HP-13Cr SS after pre-initiated.

824

825 Fig. 16 Gumbel plots of maximum pit depth for HP-13Cr SS under different

826 immersion time after pre-initiated pits at various temperature and CO₂ pressures: (a)

827 95 °C / 2.8 MPa, (b) 120 °C / 3.2 MPa, (c) 150 °C / 3.6 MPa, (d) 180 °C / 3.8 MPa

828

829 Fig. 17 Time evolution of the mean maximum pit depth fitted Gumbel distribution at

830 different temperatures and CO₂ pressures

831

832 Fig. 18 The function of pitting growth kinetics parameters K and ω with the well

833 depth

834

835 Fig. 19 Time evolution of the mean maximum pit depth fitted Gumbel distribution at

836 different flow rates

837

838 Fig. 20 Variety of pitting growth kinetics parameters K with flow rate

839

840 Fig. 21 Time evolution of the mean maximum pit depth fitted Gumbel distribution at
841 various (a) tensile stresses, and (b) compressive stresses

842

843 Fig. 22 The function of pitting growth kinetics parameters K (a) and ω (b) with the
844 stress

845

846 Fig. 23 Pareto histogram for weighing the effects of each of the factors on maximum
847 pit depth

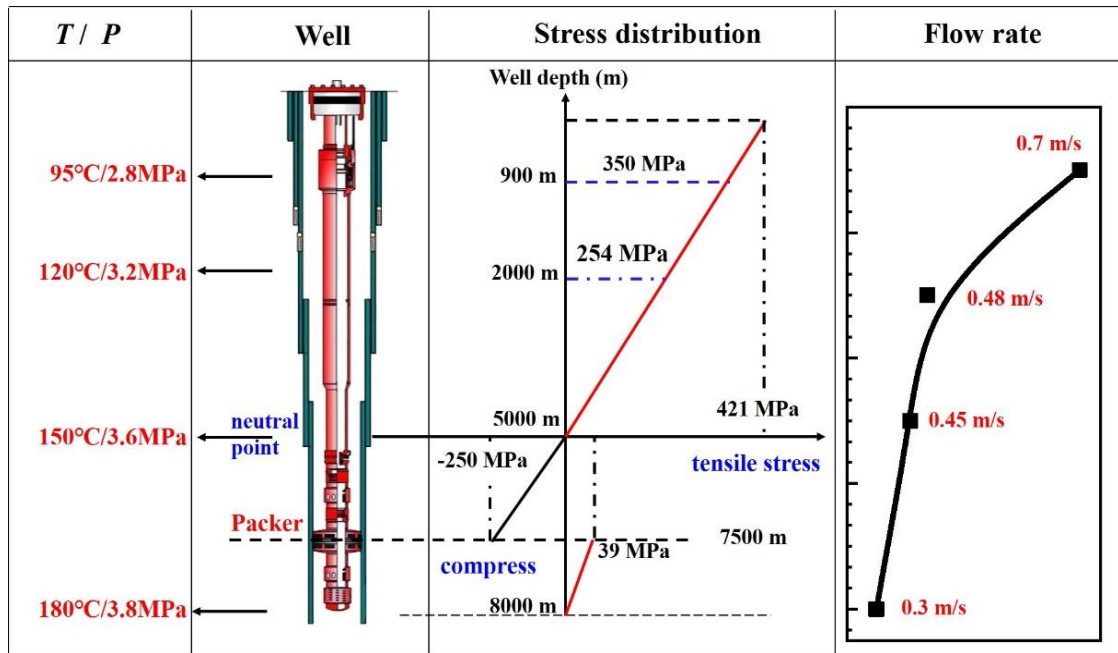
848

849 Fig. 24 Six-year-served field data and mechanistic-chemometrics model prediction
850 results for HP-13Cr SS along the well profile

851

852

853



854

855

Fig.1 Schematic diagram of complex oilfield environment

856

857

858

859

860

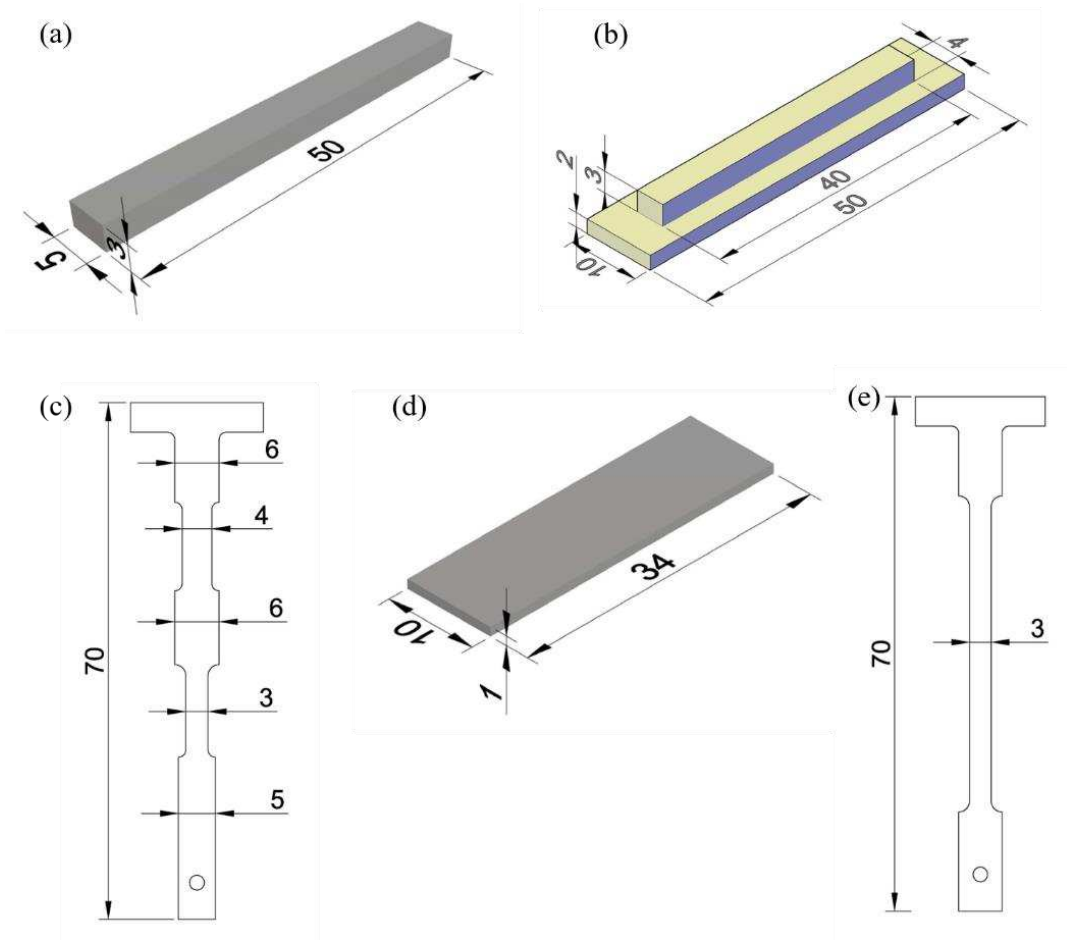
861

862

863

864

865



866

867 Fig. 2 Dimensions of the testing specimens: (a) Electrochemical and immersion

868 testing specimen, (b) bump-shaped electrode, (c) high throughput tensile stress

869 specimen, (d) compress stress specimen, (e) T-type specimen

870

871

872

873

874

875

876

877

878

879

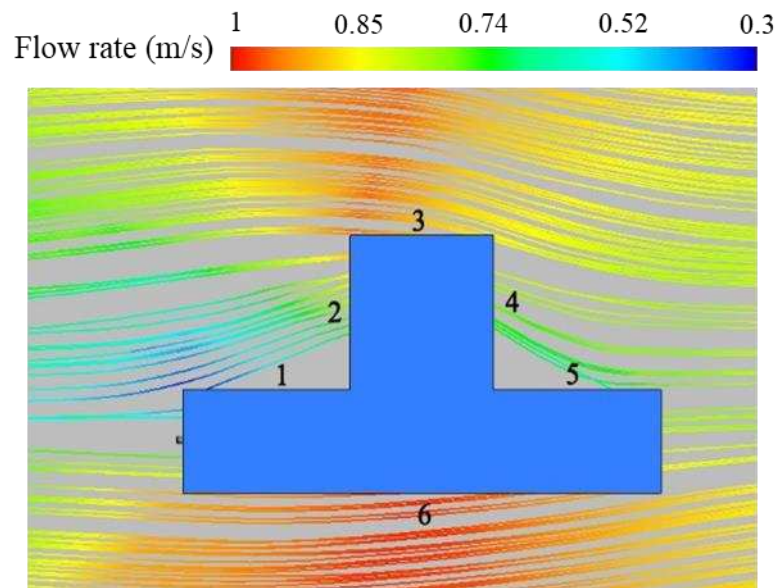
880

881

882

883

884



885

886

Fig. 3 Flow rates distribution of the bump-shaped specimen

887

888

889

890

891

892

893

894

895

896

897

898

899

900

901

902

903

904

905

906

907

908

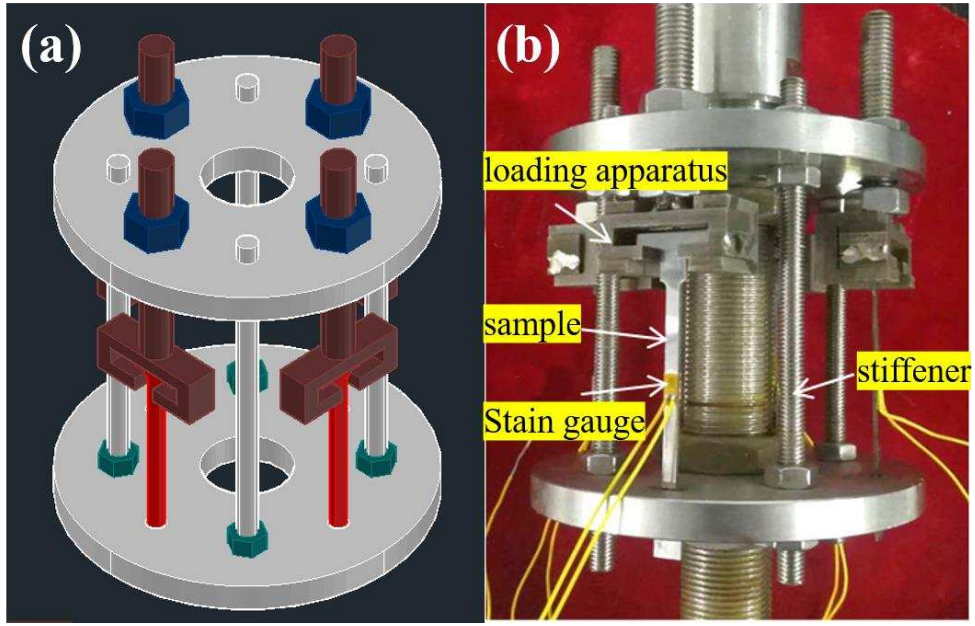
909

910

911

912

913



914

915 Fig. 4 (a) Schematic diagrams of stress corrosion rotating cage, and (b) specimen

916

assemble

917

918

919

920

921

922

923

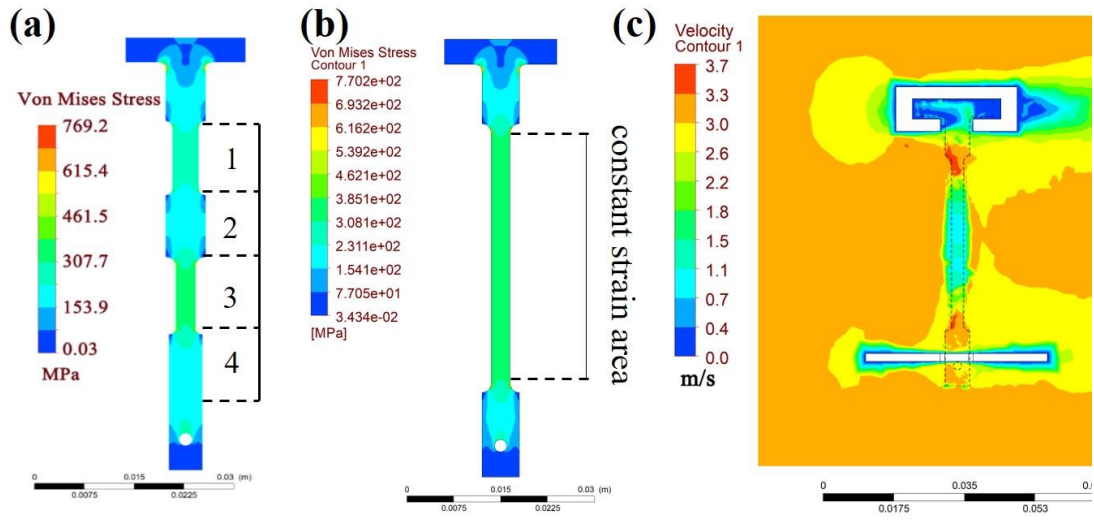
924

925

926

927

928



929

930 Fig. 5 (a) and (b) von Mises stress distribution of the flat high throughout tensile

931 stress specimen and the T-type specimen, (c) flow distribution around the T-type

932 specimen

933

934

935

936

937

938

939

940

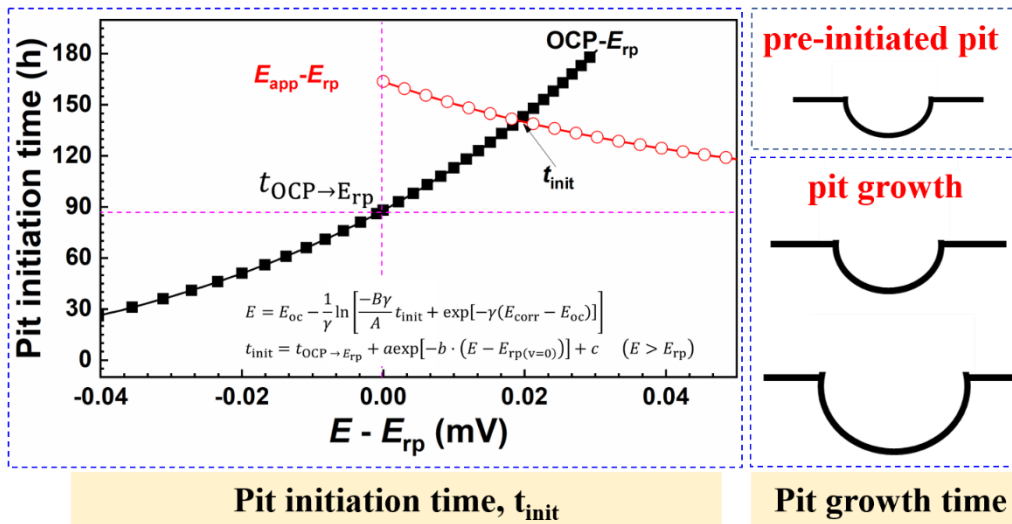
941

942

943

944

945



946

947 Fig. 6 Schematic of pitting corrosion processes to construct the pitting damage

948

prediction model.

949

950

951

952

953

954

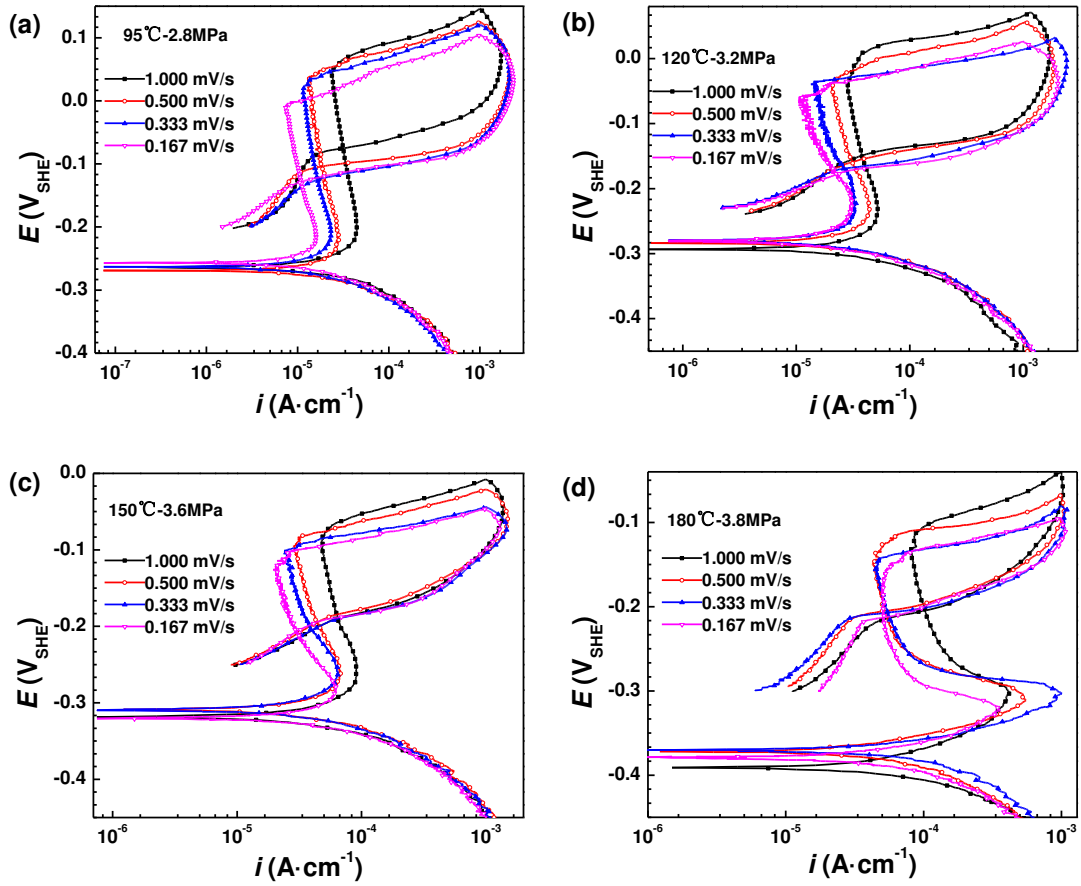
955

956

957

958

959



960

961

962

Fig. 7 Cyclic potentiodynamic polarization curves of HP-13Cr SS in simulation

963

formation water at different potential scan rates under various temperatures and CO₂

964

pressures: (a) 95 °C / 2.8 MPa, (b) 120 °C / 3.2 MPa, (c) 150 °C / 3.6 MPa, (d) 180 °C /

965

3.8 MPa

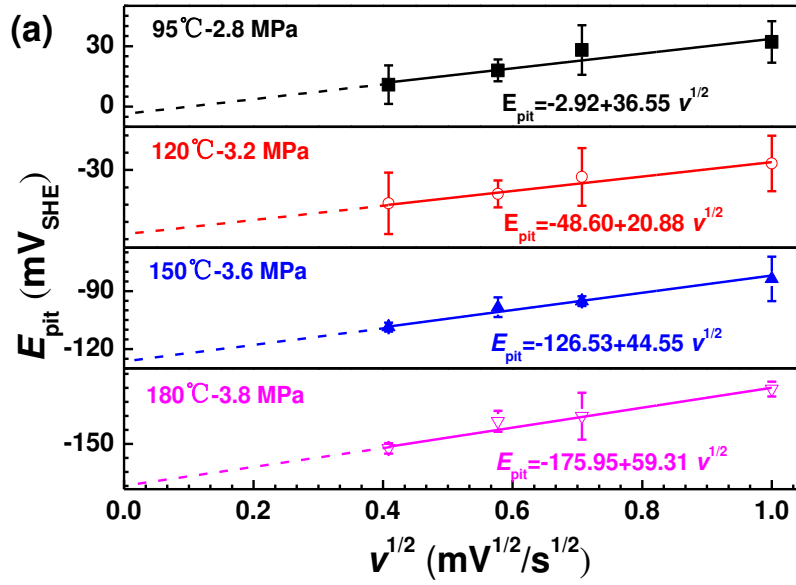
966

967

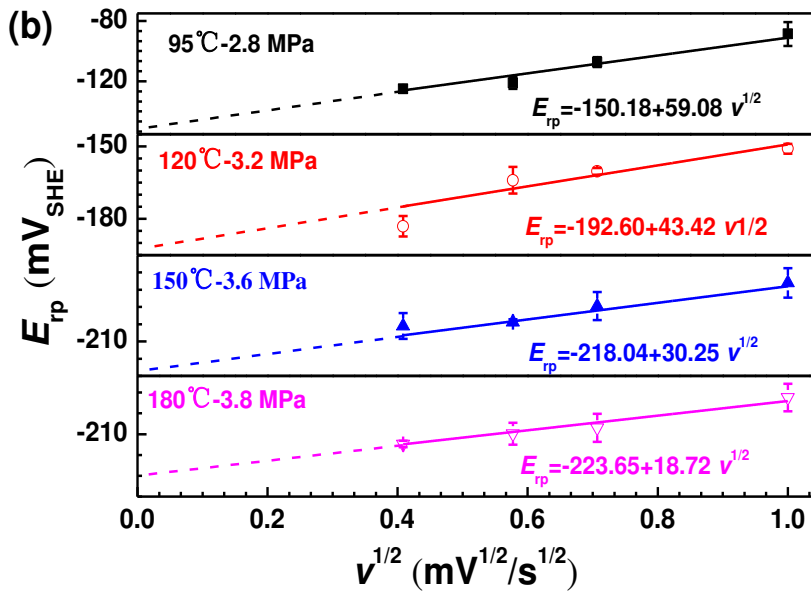
968

969

970



971



972

973 Fig. 8 E_{pit} (a) and E_{rp} (b) at different potential scan rates (v) for HP-13Cr SS in

974 formation water at different temperatures and CO₂ pressures

975

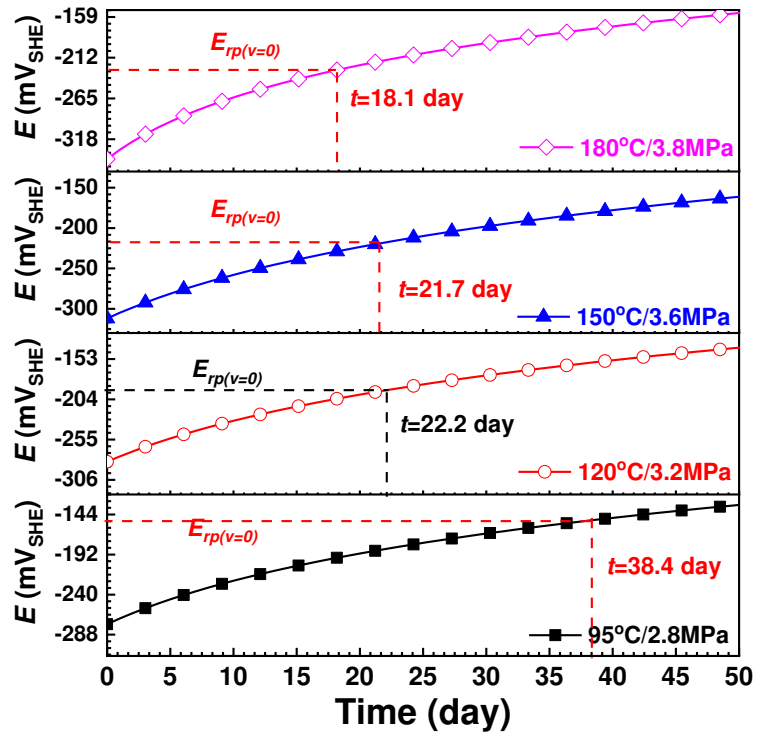
976

977

978

979

980



981

982 Fig. 9 OCP evolution of HP-13Cr SS in formation water under various temperatures

983 and CO₂ pressures

984

985

986

987

988

989

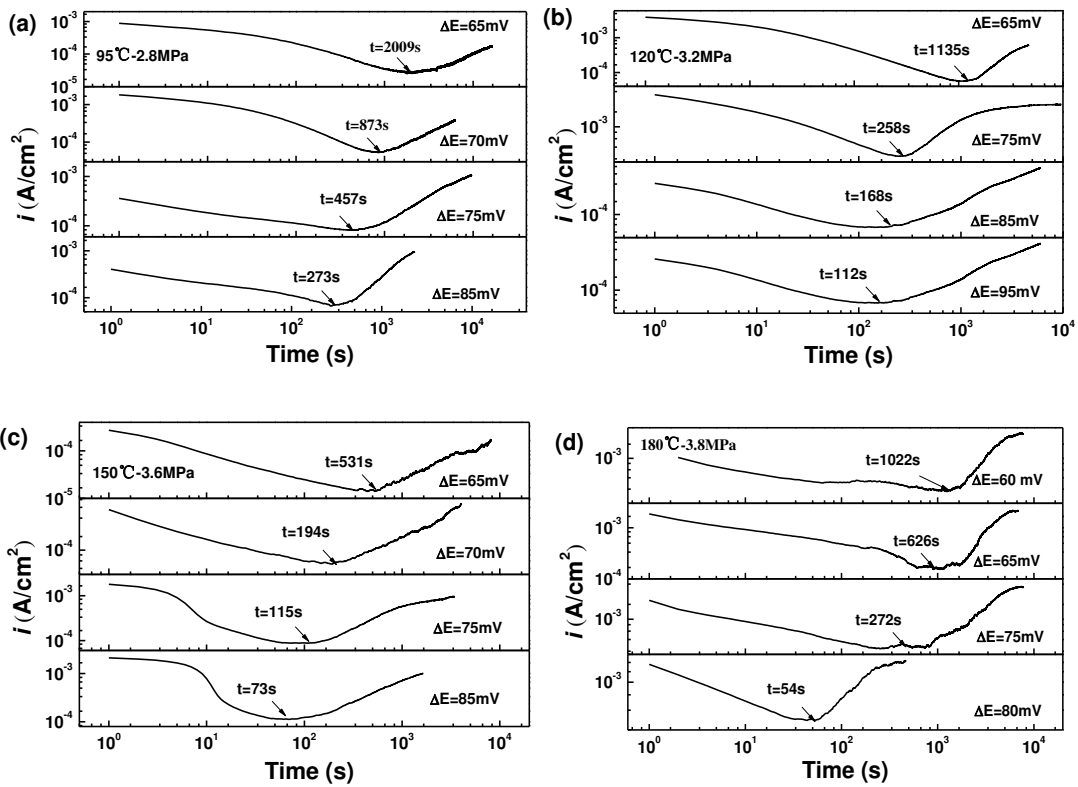
990

991

992

993

994



995

996

997 Fig.10 Variation of current density (i) with stable pit formation time of HP-13Cr SS in

998 formation water under various temperatures and CO₂ pressures: (a) 95 °C / 2.8 MPa,

999 (b) 120 °C / 3.2 MPa, (c) 150 °C / 3.6 MPa, (d) 180 °C / 3.8 MPa

1000

1001

1002

1003

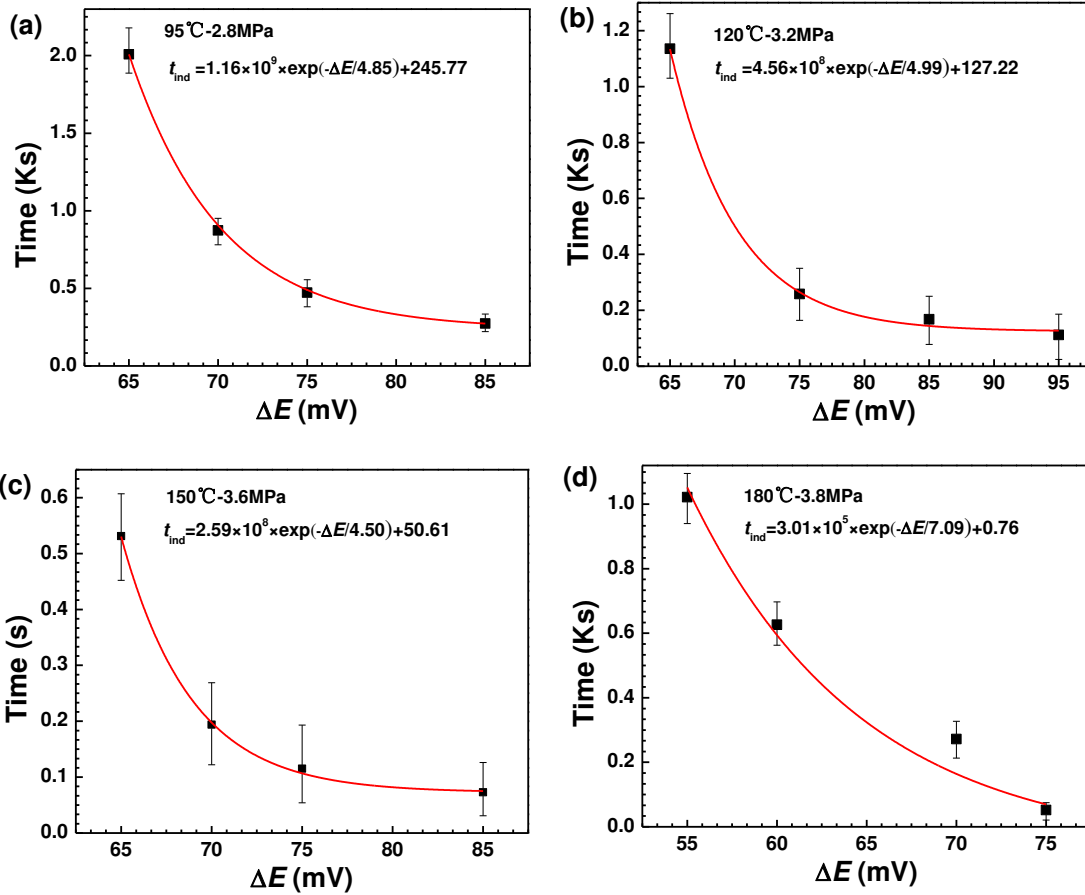
1004

1005

1006

1007

1008



1009

1010

1011

1012

1013

1014

1015

1016

1017

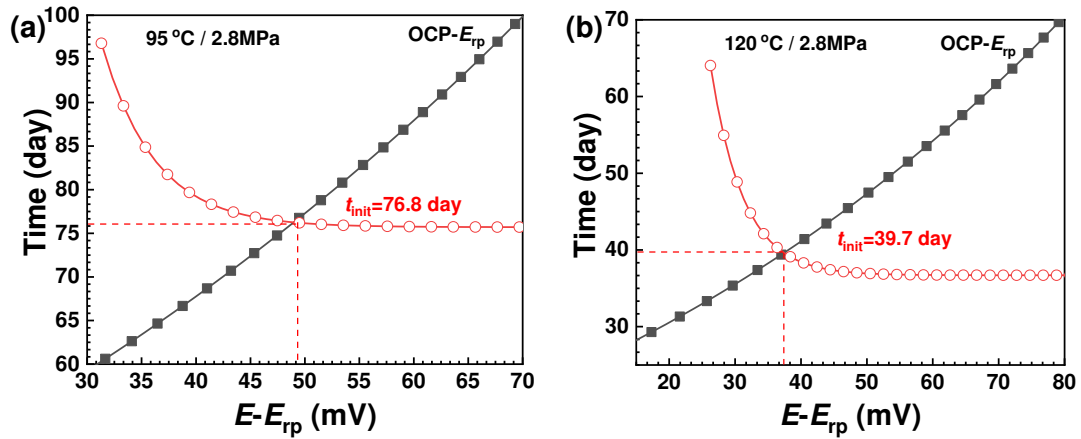
1018

1019

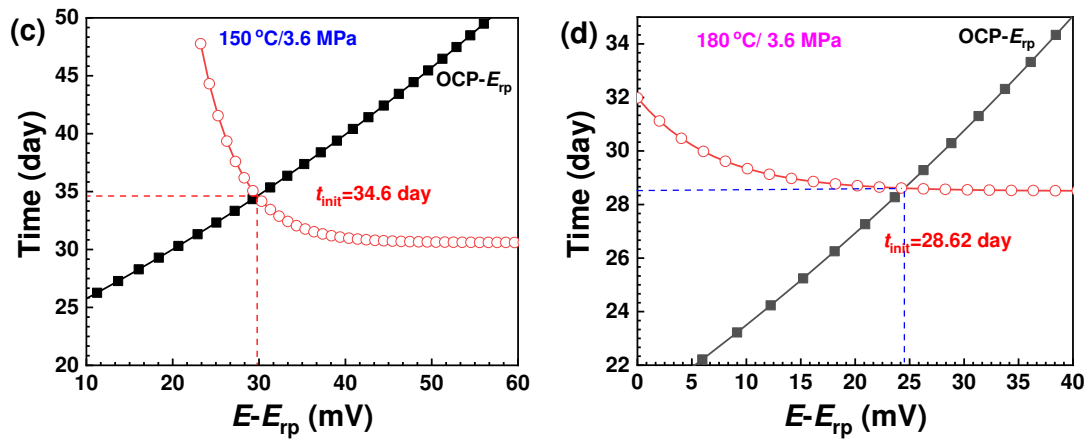
1020

Fig. 11 Variation of pit induction time with ΔE ($E_{app} - E_{rp}$) of HP-13Cr SS under various temperatures and CO₂ pressures: (a) 95 °C / 2.8 MPa, (b) 120 °C / 3.2 MPa, (c) 150 °C / 3.6 MPa, (d) 180 °C / 3.8 MPa

1021



1022



1023

1024

Fig.12 Pit initiation time of HP-13Cr SS in formation water under various

1025

temperatures and CO₂ pressures: (a) 95 °C / 2.8 MPa, (b) 120 °C / 3.2 MPa, (c) 150 °C

1026

/ 3.6 MPa, (d) 180 °C / 3.8 MPa

1027

1028

1029

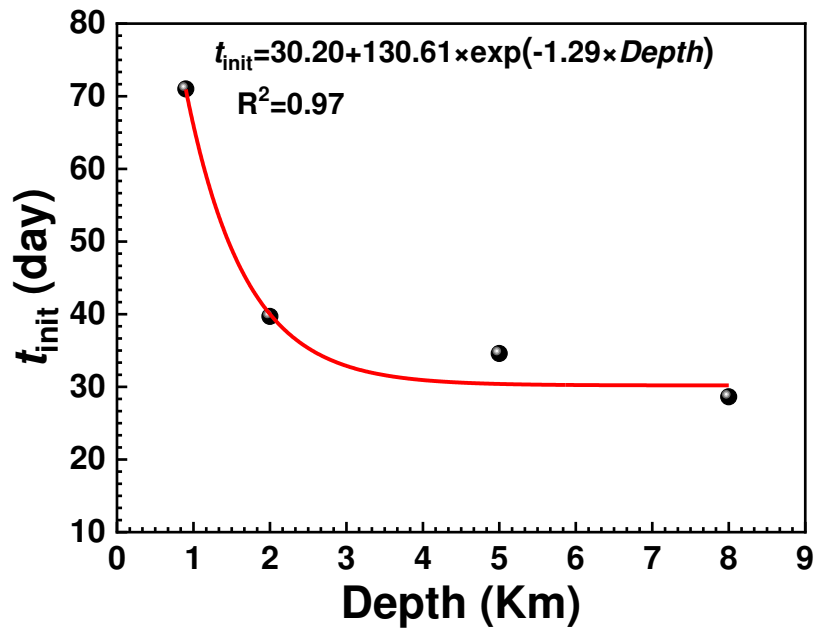
1030

1031

1032

1033

1034



1035

1036 Fig.13 Variety of pit initiation time of HP-13Cr SS in formation water with well depth

1037

1038

1039

1040

1041

1042

1043

1044

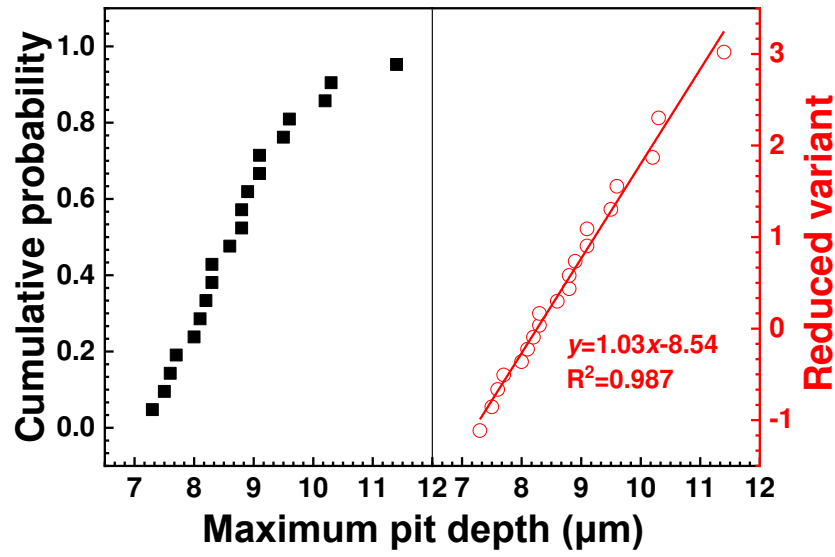
1045

1046

1047

1048

1049



1050

1051 Fig. 14 Cumulative probability and Gumbel plot of maximum pit depth for HP-13Cr

1052 SS after pre-initiated pits

1053

1054

1055

1056

1057

1058

1059

1060

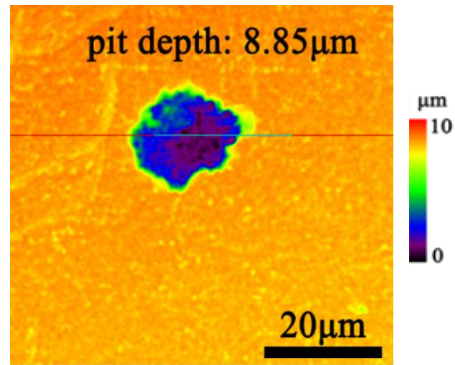
1061

1062

1063

1064

1065



1066

1067 Fig. 15 Typical morphologies of maximum pits for HP-13Cr SS after pre-initiated.

1068

1069

1070

1071

1072

1073

1074

1075

1076

1077

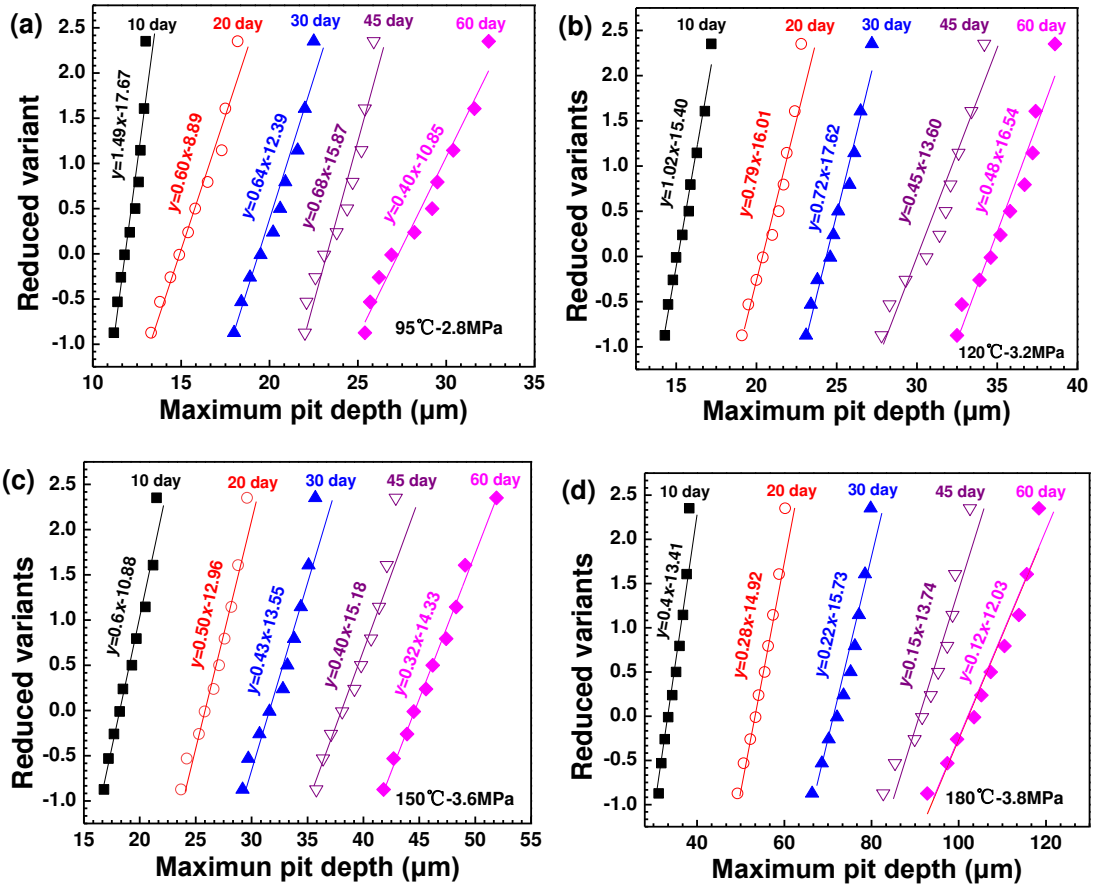
1078

1079

1080

1081

1082



1083

1084

1085

1086

1087

1088

1089

1090

1091

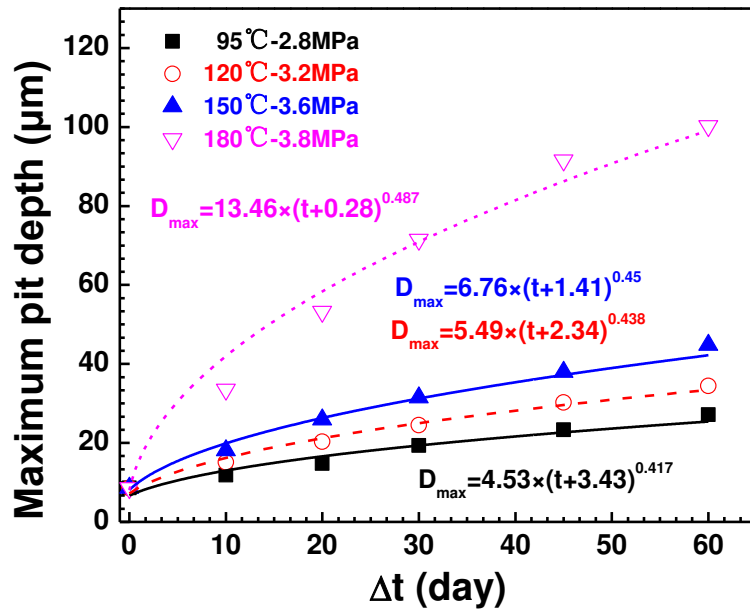
1092

1093

1094

1095

Fig. 16 Gumbel plots of maximum pit depth for HP-13Cr SS under different immersion time after pre-initiated pits at various temperature and CO₂ pressures: (a) 95 °C / 2.8 MPa, (b) 120 °C / 3.2 MPa, (c) 150 °C / 3.6 MPa, (d) 180 °C / 3.8 MPa



1096

1097 Fig. 17 Time evolution of the mean maximum pit depth fitted Gumbel distribution at

1098 different temperatures and CO₂ pressures

1099

1100

1101

1102

1103

1104

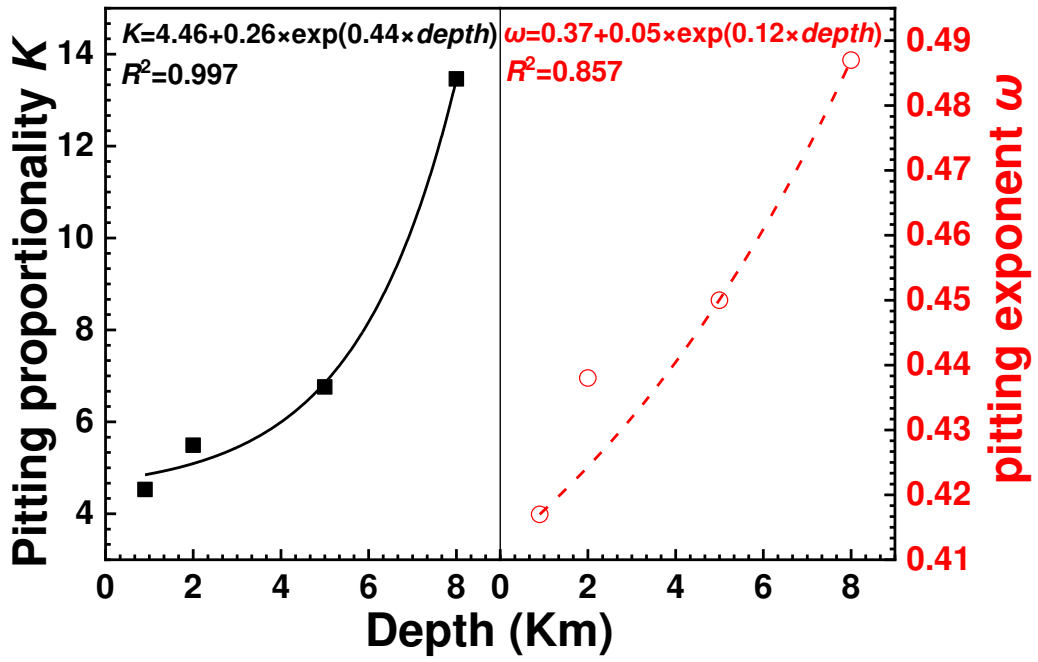
1105

1106

1107

1108

1109



1110

1111 Fig. 18 The function of pitting growth kinetics parameters K and ω with the well

1112 depth

1113

1114

1115

1116

1117

1118

1119

1120

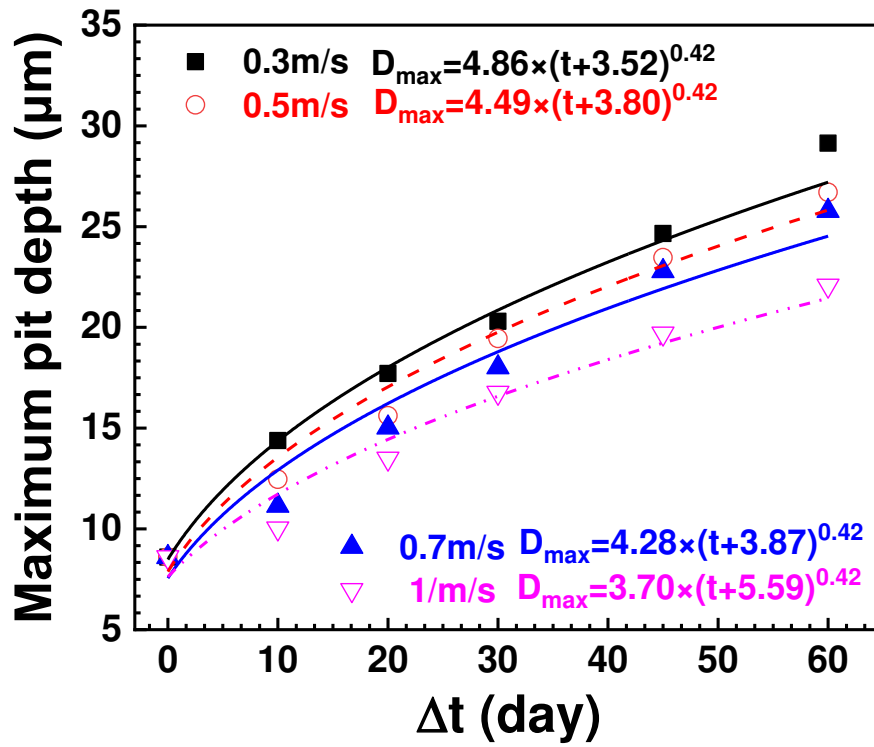
1121

1122

1123

1124

1125



1126

1127 Fig. 19 Time evolution of the mean maximum pit depth fitted Gumbel distribution at

1128 different flow rates

1129

1130

1131

1132

1133

1134

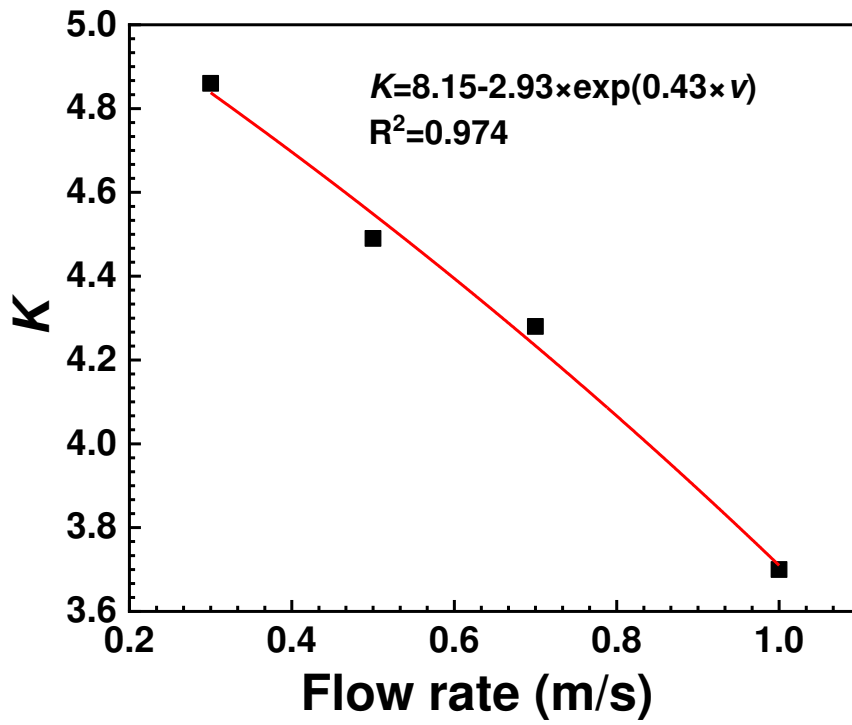
1135

1136

1137

1138

1139



1140

1141

Fig. 20 Variety of pitting growth kinetics parameters K with flow rate

1142

1143

1144

1145

1146

1147

1148

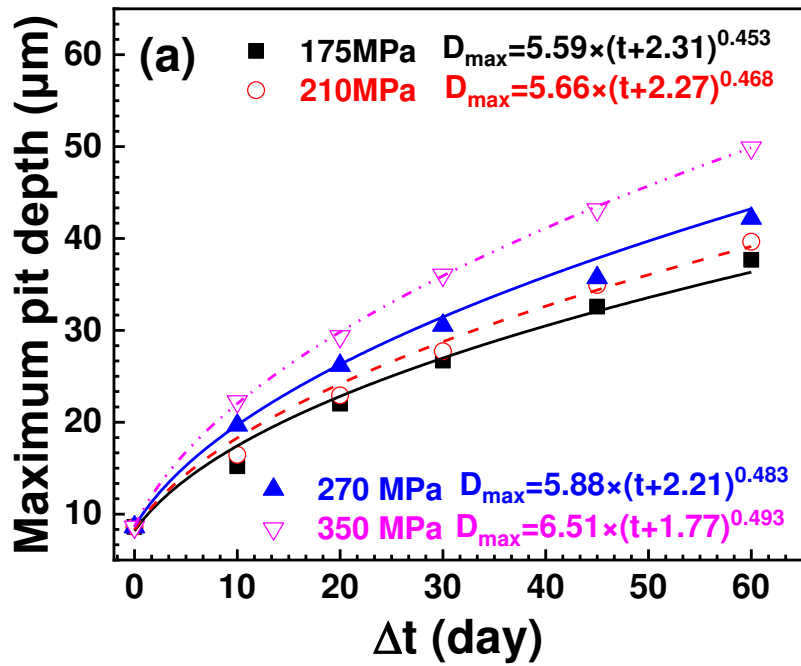
1149

1150

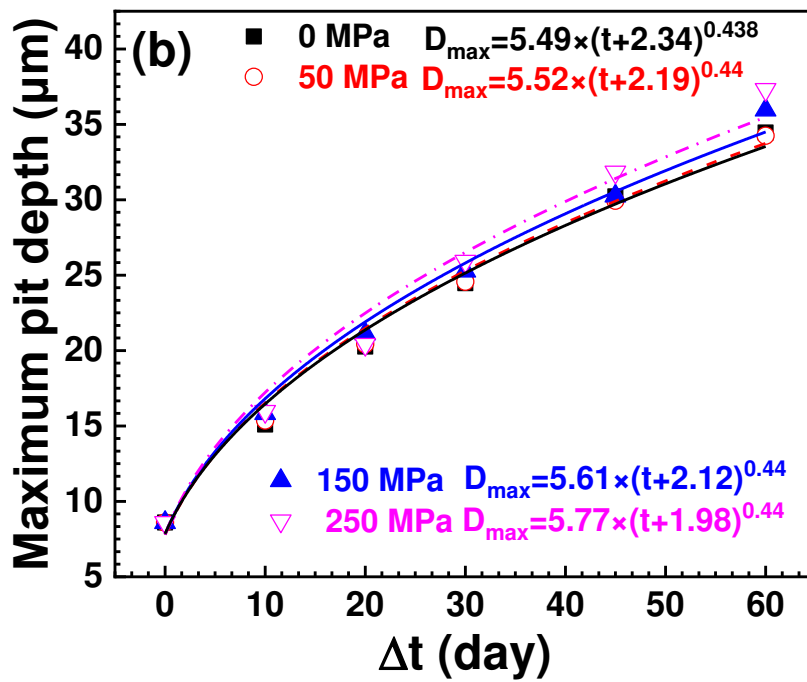
1151

1152

1153



1154



1155

1156 Fig. 21 Time evolution of the mean maximum pit depth fitted Gumbel distribution at

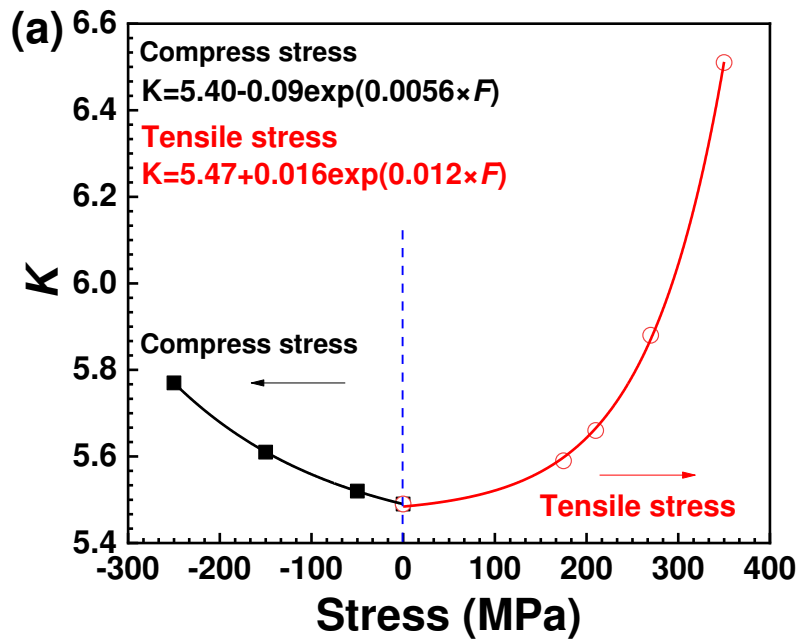
1157

various (a) tensile stresses, and (b) compressive stresses

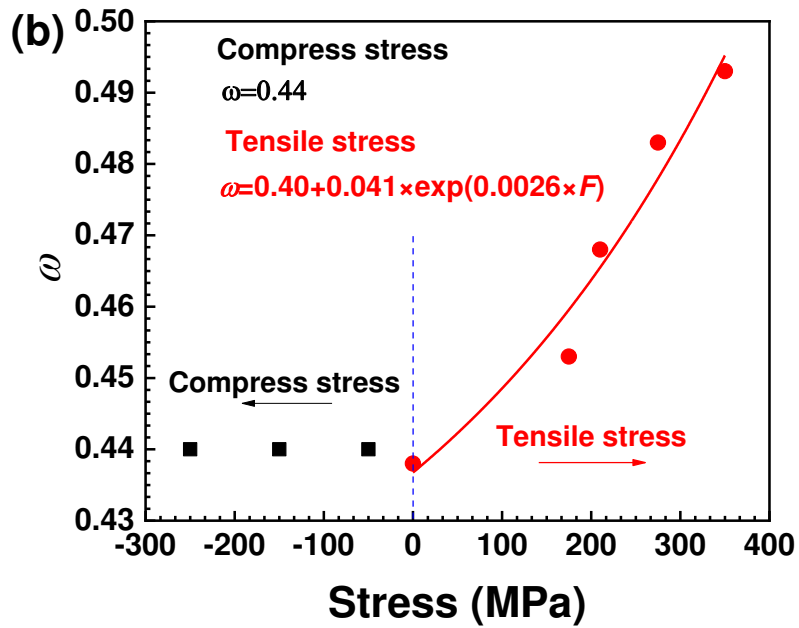
1158

1159

1160



1161



1162

1163 Fig. 22 The function of pitting growth kinetics parameters K (a) and ω (b) with the

1164

stress

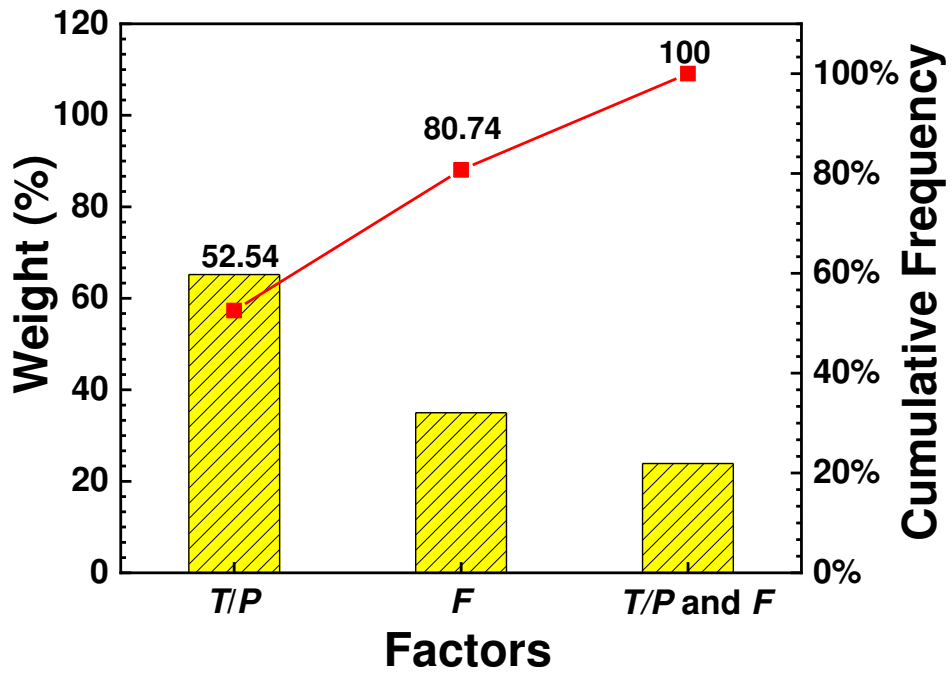
1165

1166

1167

1168

1169



1170

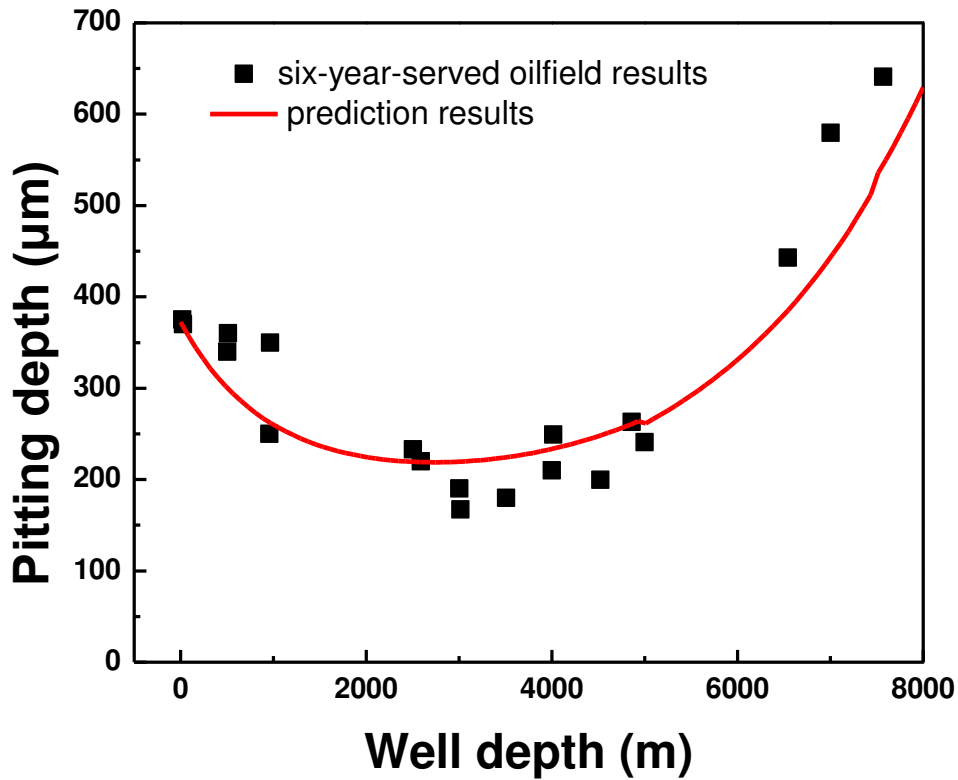
1171 Fig. 23 Pareto histogram for weighing the effects of each of the factors on maximum

1172 pit depth

1173

1174

1175



1176

1177 Fig. 24 Six-year-served field data and mechanistic-chemometrics model prediction

1178 results for HP-13Cr SS along the well profile.

1179

1180

1181 **List of tables**

1182 Table 1 Chemical composition of formation water

1183

1184 Table 2 Factor values used for factorial design including uncoded and coded form and

1185 D_{max} as the response

1186

1187 Table 3 Flow rate for each surface of the bump-shaped specimen

1188

1189 Table 4 The immersion condition of HP-13Cr SS under extremely oilfield

1190 environments

1191

1192 Table 5 The value of E_{pit} and E_{tp} at different potential sweep rate (ν) under various

1193 temperatures and CO₂ pressures

1194

1195 Table 6 Electrochemical parameters to calculate the OCP evolution of HP-13Cr SS

1196 under various temperature and CO₂ pressure

1197

1198 Table 7 Gumbel distribution fitting parameters for HP-13Cr SS at different immersion

1199 time after pre-initiated pits under various temperature and CO₂ pressure

1200

1201

1202

1203

1204

Table 1 Chemical composition of formation water

Composition	HCO ₃ ⁻	Cl ⁻	SO ₄ ²⁻	Ca ²⁺	Mg ²⁺	K ⁺	Na ⁺
Content (mg L ⁻¹)	189	60000	430	8310	561	6620	76500

1205

1206

1207

1208

1209

1210

1211

1212

1213
 1214
 1215
 1216
 1217
 1218
 1219
 1220
 1221
 1222
 1223
 1224
 1225
 1226
 1227
 1228
 1229
 1230
 1231
 1232
 1233
 1234
 1235
 1236
 1237
 1238
 1239
 1240
 1241
 1242

1243 Table 2 Factor values used for factorial design including uncoded and coded form and
 1244 D_{\max} as the response.

Experiment sequence	Factor A (T / P)	Factor B (<i>V</i>)	Factor B (<i>F</i>)	Response (D_{\max})			
	°C / MPa	m/s	MPa	μm			
1	95/2.8 (-1)	0.3 (-1)	-250 (-1)	5.59	5.84	5.32	5.74
2	95/2.8 (-1)	0.7 (+1)	-250 (-1)	5.25	5.02	5.65	5.27
3	95/2.8 (-1)	0.3 (-1)	350 (+1)	7.25	7.94	8.94	8.06

4	95/2.8 (-1)	0.7 (+1)	350 (+1)	7.07	7.21	7.66	7.32
5	180/3.8 (+1)	0.3 (-1)	-250 (-1)	13.26	14.82	15.33	15.74
6	180/3.8 (+1)	0.7 (+1)	-250 (-1)	12.28	13.06	12.08	13.28
7	180/3.8 (+1)	0.3 (-1)	350 (+1)	25.03	27.28	28.82	27.22
8	180/3.8 (+1)	0.7 (+1)	350 (+1)	23.37	24.46	25.36	22.44

1245 where temperature / CO₂ pressure represented by T / P , flow rate represented by V , stress
1246 represented by F , and the maximum pitting depth represented by D_{max} . Also, -237 MPa in factor
1247 represented compress stress, and 350 MPa represent tensile stress.

1248
1249
1250
1251
1252
1253
1254
1255
1256
1257
1258
1259
1260
1261
1262
1263
1264

1265 Table 3 Flow rate for each surface of the bump-shaped specimen

	1	2	3	4	5	6
Flow rate (m/s)	0.31	0.72	0.85	0.66	0.50	1

1266
1267
1268
1269
1270
1271
1272

1273
1274
1275
1276
1277
1278
1279
1280
1281
1282
1283
1284
1285
1286
1287
1288
1289
1290
1291
1292
1293
1294
1295
1296
1297
1298
1299
1300
1301
1302

1303 Table 4 The immersion condition of HP-13Cr SS under extremely oilfield
1304 environments

Num ber	Temperature (°C)/ Pressure (MPa)	Velocity (m/s)	Stress (MPa)
1	95 °C/2.8 MPa	0	0
2	120 °C/3.2 MPa	0	0
3	150 °C/3.6 MPa	0	0
4	180 °C/3.8 MPa	0	0

5	120 °C/3.2 MPa	0.31	0
6	120 °C/3.2 MPa	0.50	0
7	120 °C/3.2 MPa	0.72	0
8	120 °C/3.2 MPa	1	0
9	120 °C/3.2 MPa	0	175
10	120 °C/3.2 MPa	0	210
11	120 °C/3.2 MPa	0	270
12	120 °C/3.2 MPa	0	350

1305
1306
1307
1308
1309
1310
1311
1312
1313
1314
1315
1316
1317
1318
1319
1320
1321
1322
1323
1324

1325 Table 5 The value of E_{pit} and E_{tp} at different potential sweep rate (ν) under various
1326 temperatures and CO₂ pressures

ν (mV/s)		95 °C/2.8 MPa	120 °C/3.2 MPa	150 °C/3.6 MPa	180 °C/3.8 MPa
E_{pit}	1.000	32.04 ± 10.29	-28.08 ± 8.03	-83.69 ± 11.5	-117.39 ± 4.42
(mV _{SHE})	0.500	28.08 ± 12.26	-32.03 ± 8.34	-95.2 ± 2.48	-133.53 ± 13.99

	0.333	17.98 ± 5.39	-36.94 ± 3.89	-98.37 ± 5.06	-136.57 ± 6.27
	0.167	10.89 ± 9.58	-39.61 ± 8.89	-108.63 ± 2.32	-152.66 ± 3.13
	0	-2.92	-48.60	-126.53	-175.95
E_{tp} (mV _{SHE})	1.000	-88.67 ± 7.83	-150.96 ± 2.05	-193.01 ± 4.29	-201.21 ± 3.31
	0.500	-107.28 ± 3.25	-160.34 ± 1.42	-199.73 ± 4.07	-208.48 ± 3.39
	0.333	-121.07 ± 3.91	-164.05 ± 5.52	-204.37 ± 0.81	-209.89 ± 2.62
	0.167	-125.07 ± 2.34	-183.1 ± 4.21	-205.51 ± 3.74	-212.38 ± 0.78
	0	-150.18	-192.60	-218.04	-223.65

1327
1328
1329
1330
1331
1332
1333
1334
1335
1336
1337
1338
1339
1340
1341
1342
1343

1344 Table 6 Electrochemical parameters to calculate the OCP evolution of HP-13Cr SS
1345 under various temperature and CO₂ pressure

	γ (mV·dec ⁻¹)	i_o (A·cm ⁻²)	E_{oc} (mV)	ϵ_L (V·cm ⁻¹)	E_{corr} (mV)
95 °C / 2.8 MPa	-89.36	4.93×10^{-5}	-182.7	7.38×10^3	-275.6
120 °C / 3.2	-92.67	5.99×10^{-5}	-155.1	6.04×10^3	-282.4

MPa						
150 °C / 3.6	-97.37	4.11×10^{-5}			4.96×10^3	
				-117.0		-312.1
MPa						
180 °C / 3.8	-91.07	2.28×10^{-5}			84	
				-72.8		-344.5
MPa						

1346
1347
1348
1349
1350
1351
1352
1353
1354
1355
1356
1357
1358
1359
1360
1361
1362
1363
1364
1365
1366
1367
1368
1369
1370
1371
1372
1373
1374
1375

1376 Table 7 Gumbel distribution fitting parameters for HP-13Cr SS at different immersion
1377 time after pre-initiated pits under various temperature and CO₂ pressure

Temperature and CO ₂ pressure	Time (day)	Scale parameter (λ)	Local parameter (μ) μm
95 °C / 2.8 MPa	10	0.67	11.85
	20	1.66	14.82
	30	1.56	19.36
	45	1.47	23.34
	60	2.50	27.13
120 °C / 3.2 MPa	10	0.98	15.10
	20	1.27	20.27
	30	1.39	24.47
	45	2.22	30.22
	60	2.08	34.46
150 °C / 3.6 MPa	10	1.67	18.13
	20	2.00	25.92
	30	2.33	31.51
	45	2.50	37.95
	60	3.13	44.78
180 °C / 3.8 MPa	10	0.25	33.53
	20	3.57	53.29
	30	4.55	71.50
	45	6.67	91.6
	60	8.33	100.25

1378

1379

1380

1381

1382

1383

1384

1385